

國立交通大學

理學院 應用化學系

碩士論文

Department of Applied Chemistry, College of Science

National Chiao Tung University

Master of science degree thesis

Towards the Analysis of Small Molecules
with High Spatial and Temporal Resolution

使用高空間及高時間解析方法應用於
小分子之分析

研究生： 李柏翰

Student: Po-Han Li

指導教授： 帕偉鄂本 博士

Advisors: Dr Pawel L. Urban

陳月枝 博士

Dr Yu-Chie Chen

Hsinchu — July 2012

Towards the Analysis of Small Molecules
with High Spatial and Temporal Resolution

使用高空間及高時間解析方法應用於小分子之分析

研究生： 李柏翰

Student: Po-Han Li

指導教授： 帕偉鄂本 博士

Advisors: Dr Pawel L. Urban

陳月枝 博士

Dr Yu-Chie Chen



A thesis Submitted to the M.S. progress, Department of Applied Chemistry,
College of Science,
National Chiao Tung University,
in partial fulfillment of the requirements
for the Degree of Master of Science in Applied Chemistry

July 2012

Hsinchu, Taiwan, Republic of China

Hsinchu, July, 2012

使用高空間及高時間解析方法應用於小分子之分析

研究生： 李柏翰

指導教授： 帕偉鄂本 博士

陳月枝 博士

國立交通大學應用化學系 碩士班

摘要

在分析化學領域中，發展出具高空間及高時間解析分析方法已成為日益重要的課題，例如在基質輔助雷射脫附游離質譜影像分析中，提升空間解析有助於將質譜影像到達微米等級的解析度；而提高時間解析也有利於各種化學動力學之即時偵測與探討。

在本論文中，首先我們發展出一種能應用在基質輔助雷射脫附游離質譜影像分析的有機無機混合材料奈米粒子。此奈米粒子為含有基質輔助雷射脫附游離質譜基質的矽球，其表面帶有正電荷，能藉由靜電吸引力吸附在帶有負電荷的生物樣品(藻類)上，接著在使用氬水蒸汽將奈米粒子中基質輔助雷射脫附游離質譜的基質釋放出來。使用本論文開發出的奈米粒子配合光徑 10 μm 的紫外光雷射對樣品進行脫附游離，在基質輔助雷射脫附游離質譜影像分析能達到 15 μm 左右的高空間解析度質譜影像結果。

在本論文的第二部份，我們自行組裝出一種能同時進行多點和多探測光源偵測的光學儀器；利用此光學儀器結合間隔式和連續式進樣法，我們成功達成監控分析物在溶液中對流情形的線上即時偵測。此外，本論文開發的光學儀器可與電噴灑游離法離子阱質譜儀進行串聯，接著配合連續式進樣法進樣來監測分析物對流情形，我們也成功的同時利用本論文所裝設的系統得到吸收光譜和質量分析的線上即時偵測結果。相信本論文開發出的實驗方法在未來能對自然界很多物理現象的討探會有很好的貢獻。

Towards the Analysis of Small Molecules with High Spatial and Temporal Resolution

Student: Po-Han Li

Advisors: Dr Pawel L. Urban

Dr Yu-Chie Chen

M. S. progress, Department of Applied Chemistry, National Chiao Tung University

Abstract

Development of analytical methods with high spatial resolution and high temporal resolution has become an important goal in analytical chemistry. For example, matrix-assisted laser desorption/ionization (MALDI) mass spectrometry (MS) enables mapping chemical molecules in two-dimensional samples with a micrometer-range spatial resolution. On the other hand, fast detection techniques are introduced to accommodate the analysis of dynamic chemical systems. In this work, we demonstrate hybrid nanoparticles which can facilitate mass spectrometric imaging at high spatial resolution. The nanoparticles attach to biological specimens (algal cells) due to electrostatic interactions, which is further followed by a controlled release of an organic MALDI matrix in the presence of alkaline vapors of ammonia. Using this method – in conjunction with a MALDI-MS instrument equipped with a 10- μm ultraviolet laser beam – we achieved the spatial resolution of approximately 15 μm . In the second part – in order to preserve temporal resolution – we implemented an on-line sampling system which takes advantage of segmented or continuous flow. The system was used in conjunction with a home-made multi-point multi-wavelength optical detector. The device enabled real-time monitoring of convection currents. The continuous flow sampling, and the optical detector, were readily hyphenated with an electrospray ion-trap mass spectrometer. This enabled online analysis of the low-volume liquid samples collected from the convection vessel – simultaneously – by light absorption and mass spectrometry. We believe that the developments presented here will contribute to new discoveries in natural and physical sciences.

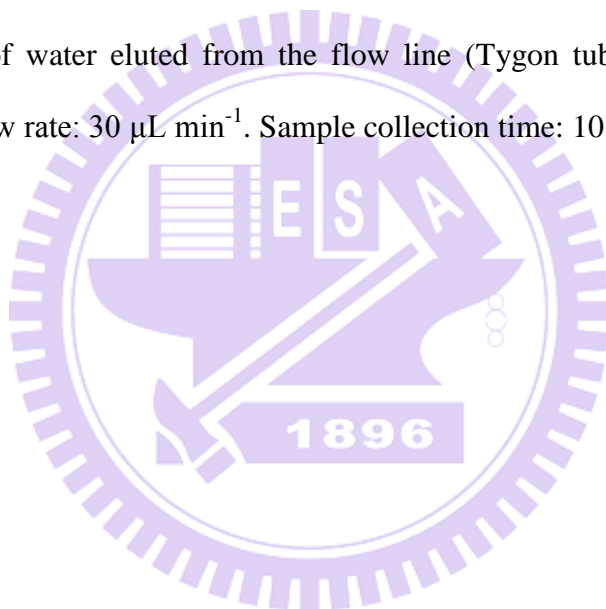
Table of contents

List of tables.....	V
List of figures.....	VI
Acknowledgements.....	XV
Chapter 1. Introduction.....	1
1.1. Foreword.....	1
1.2. Matrix-assisted laser desorption/ionization mass spectrometry.....	2
1.2.1. Principles of matrix-assisted laser desorption/ionization.....	2
1.2.2. MALDI matrix.....	3
1.2.3. Time-of-flight mass analyzer.....	3
1.2.4. MALDI imaging.....	4
1.3. Electrospray ionization mass spectrometry.....	4
1.3.1. Principles of electrospray ionization.....	4
1.3.2. Ion-trap mass analyzer.....	6
1.4. Optical absorption detection.....	7
1.5. Segmented flow.....	9
1.6. Goals of the work.....	11
Chapter 2. Hybrid nanoparticles for mass spectrometric imaging of single cells. 13	13
2.1. Introduction.....	13
2.2. Materials and methods.....	14
2.2.1. Materials.....	14
2.2.2. Synthesis SiO ₂ /9-AA and SiO ₂ nanoparticles.....	14
2.2.3. The controlled release of 9-AA from SiO ₂ /9-AA nanoparticles by alkali.	15
2.2.4. Preparation of algal cells for analysis.....	16
2.2.5. Controlled release of 9-AA by exposure to ammonia vapors.....	17

2.2.6.	MALDI-MS and MALDI imaging.....	18
2.3.	Results and discussion.....	19
2.3.1.	Synthesis and initial testing of the hybrid nanoparticles.....	19
2.3.2.	Evaluation of the controlled matrix release process.....	20
2.3.3.	Application in the imaging of single cells.....	22
2.4.	Concluding remarks.....	32
Chapter 3.	Recording temporal characteristics of convection currents by continuous and segmented-flow sampling.....	34
3.1.	Introduction.....	34
3.2.	Materials and methods.....	36
3.2.1.	Materials.....	36
3.2.2.	Construction of the flow-through optical detector.....	36
3.2.3.	Assembly of the three-port Y-junction for generating segmented flow....	38
3.2.4.	Measurements using the system coupled with a mass spectrometer.....	38
3.2.5.	Measurement of the flow rate in the ESI emitter.....	40
3.3.	Results and Discussion.....	41
3.3.1.	Monitoring convection-driven currents by optical detector.....	41
3.3.2.	Monitoring convection-driven currents by optical detector and mass spectrometer.....	47
3.4.	Concluding remarks.....	50
Chapter 4.	Conclusions.....	53
	References.....	55

List of tables

- Table 1.1** Matching the observed and the predicted m/z values after the analysis of *Closterium acerosum* cells by negative-ion MALDI-TOF-MS using 9-aminoacridine as matrix, and in the presence of internal calibrants. The internal calibrant mixture contained adenosine triphosphate, guanosine triphosphate, uridine diphosphate glucose, acetyl coenzyme A and bradykinin acetate (each at the concentration of 8.33×10^{-6} M)..... 30
- Table 2.1** Measurement of flow rate in the system depicted in Figure 2.1 by weighing aliquots of water eluted from the flow line (Tygon tubing ID 0.13 mm). Preset flow rate: $30 \mu\text{L min}^{-1}$. Sample collection time: 10 min..... 50



List of figures

Figure 1.1	The process of desorption/ionization in MALDI. Figure reproduced from reference 3.....	2
Figure 1.2	The principle of MALDI imaging. (A) A sample containing bradykinin acetate ($[M+H]^+$ at m/z 1058.5) is used to write “Leebo” on a MALDI sample plate. (B) Matrix is coated on top of the sample plate. (C) UV laser beam is raster-scanner over the sample. The sampling sites are indicated with red circles. If a site illuminated by the laser beam contains bradykinin acetate, a signal at the m/z 1058.5 (in the positive-ion mode) will be recorded. (D) The spectra collected in (C) are converted to a molecular map depicting the distribution of bradykinin on the plate surface.....	5
Figure 1.3	The process of electrospray ionization. Figure reproduced from reference 37.....	6
Figure 1.4	The structure in an ion trap. Figure reproduced from reference 41.....	7
Figure 1.5	The incident light (P_0) passes through a sample; the light beam intensity after the optical cell is lower than that of the incident light beam ($P_1 < P_0$) which shows that the sample is not completely transparent to light at the wavelength used. The length b is the optical pathlength. The point SP is a sampling point described in section 1.4.....	9
Figure 1.6	Dispersion of a sample plug in the continuous (hydrodynamic) flow. Figure reproduced from reference 26.....	10
Figure 1.7	Methods for producing segmented flow. Figure reproduced from reference 29.....	11

Figure 1.8	Separation of individual segments of samples (grey to black) with air bubbles (white) along the flow line; mixing of the transported liquid within the segments (arrows). Figure reproduced from reference 30.....	11
Figure 2.1	Synthesis of the hybrid SiO ₂ /9-AA nanoparticles.....	15
Figure 2.2	Preparation of cells for mass spectrometric imaging.....	17
Figure 2.3	Setup for the controlled release of 9-AA in the presence of gaseous ammonia.....	18
Figure 2.4	Scanning electron micrographs of the hybrid SiO ₂ /9-AA nanoparticles (A and B) as well as single-component SiO ₂ nanoparticles (C and D). (A) SiO ₂ /9-AA nanoparticles (as synthesized). (B) SiO ₂ nanoparticles (without 9-AA) synthesized using 3 mL 33% NH ₃ (aq). (C) SiO ₂ nanoparticles (without 9-AA) synthesized using 4 mL 33% NH ₃ (aq).....	20
Figure 2.5	The effect of ammonia vapors (NH ₃ (g)) on signal intensity and signal-to-noise (<i>S/N</i>) ratio in MALDI-MS analysis of a chemical standard solution (1 μL) containing adenosine triphosphate (ATP), guanosine triphosphate (GTP), uridine diphosphate glucose (UDP-Glc) and 1,2-dipalmitoyl- <i>sn</i> -glycero-3-[phospho- <i>rac</i> -α-glycerol] (PG) using SiO ₂ /9-AA nanoparticles as matrix. The sample/nanoparticle deposits in (A) and (C) were not incubated with NH ₃ (g) while the sample/nanoparticle deposits in (B) and (D) were incubated with NH ₃ (g). Analyte concentrations in (A and B): ATP, GTP, and UDP-Glc – each 2.5 × 10 ⁻⁵ M; PG – 3.6 × 10 ⁻⁵ M. Analyte concentrations in (C and D): ATP, GTP, and UDP-Glc – each 2.5 × 10 ⁻⁶ M; PG – 3.6 × 10 ⁻⁶ M. Peak identities: ATP, <i>m/z</i> 506.0; GTP <i>m/z</i> 522; UDP-Glc, <i>m/z</i> 565; PG, <i>m/z</i> 721.5.....	21

Figure 2.6 Optical micrographs of dry deposits of different samples on an aluminum plate used as MALDI target: (A) 2 μL of 1:1 (v/v) mixture of 9 mg mL^{-1} 9-AA solution in acetone and 10^{-5} M adenosine triphosphate in water; (B) 2 μL 10^{-5} M solution of adenosine triphosphate was allowed to dry, followed by deposition of 0.5 μL suspension of the $\text{SiO}_2/9\text{-AA}$ nanoparticles (5 mg mL^{-1}). (C) Micrograph showing the edge of the $\text{SiO}_2/9\text{-AA}$ nanoparticle deposit on the aluminum plate (same as in (B)). Hybrid $\text{SiO}_2/9\text{-AA}$ nanoparticles provide unprecedented homogeneity of the matrix deposit on the microscopic level (B and C), as compared with the heterogeneous crystalline deposit of 9-AA (A). Scale bars: 200 μm 22

Figure 2.7 Controlled release of 9-AA in the liquid phase. (A and B) Fluorescence spectra ($\lambda_{\text{ex}} = 400 \text{ nm}$) of supernatants collected from the $\text{SiO}_2/9\text{-AA}$ nanoparticle suspensions. (A) Leaching 9-AA from the $\text{SiO}_2/9\text{-AA}$ nanoparticles by addition of 10 μL of 33% $\text{NH}_3(\text{aq})$ to 200 μL of the 0.5 mg mL^{-1} nanoparticle suspension in 50% ethanol. The pH of the resulting suspension was ~ 14 . (B) Leaching 9-AA from the $\text{SiO}_2/9\text{-AA}$ nanoparticles with 10 μL of pure water. The black lines in (A) and (B) correspond to the supernatant from the 1st washing step, and the red and blue lines correspond to the supernatants obtained after the 2nd and the 3rd washing step, respectively. (C) Photographs of 0.6-mL microcentrifuge tubes containing $\text{SiO}_2/9\text{-AA}$ nanoparticles – after washing with $\text{NH}_3(\text{aq})/\text{water}$, and centrifugation (10000 rpm, 10 min). Note that the pellets became pale after the treatment with $\text{NH}_3(\text{aq})$ (C), which indicates the 9-AA had been leached from the $\text{SiO}_2/9\text{-AA}$ nanoparticles..... 23

Figure 2.8	Scanning electron micrographs of SiO ₂ /9-AA nanoparticles following incubation in NH ₃ (aq) solution for 30 min.....	24
Figure 2.9	Putative mechanism of the adsorption of SiO ₂ /9-AA nanoparticles on algal cells, followed by the controlled release of 9-AA.....	25
Figure 2.10	Optical and fluorescence micrographs of individual <i>Closterium acerosum</i> cells with/without SiO ₂ /9-AA nanoparticles. Scale bars: 200 μm.....	25
Figure 2.11	Optical and fluorescence micrographs of <i>Anabaena</i> sp. with/without SiO ₂ /9-AA nanoparticles (0.5 μL, 5 mg mL ⁻¹). The fluorescence micrographs were obtained using two different excitation wavelengths (λ_{ex} = 510-560 and 330-380 nm – middle and right, respectively). Blue arrows indicate heterocysts. Scale bars: 50 μm.....	26
Figure 2.12	Single-cell MS imaging with SiO ₂ /9-AA nanoparticles used as matrix. (A) Optical and fluorescence micrographs of a single <i>Closterium acerosum</i> cell with the attached SiO ₂ /9-AA nanoparticles. (B) MALDI mass spectrum of a single cell of <i>Closterium acerosum</i> – following the occlusion with SiO ₂ /9-AA nanoparticles, and the release of 9-AA induced by gaseous ammonia. The blank spectrum of SiO ₂ /9-AA nanoparticles shows no peaks overlapping with the three sample-related peaks (Figure 2.13). (C) Mass spectrometric images of a single cell of <i>Closterium acerosum</i> (same as in (A)). The MS images were obtained in the negative-ion mode by MALDI-time-of-flight (TOF)-MS. Laser beam wavelength: 355 nm; frequency: 50 Hz; diameter: 10 μm; raster spacing: 15 μm. The red-color dashed line in (A) approximately delimits the MS imaging area in (C). Scale bars: 200 μm.....	27

- Figure 2.13** MALDI mass spectrum of SiO₂/9-AA nanoparticles deposited on an aluminum plate, and incubated with gaseous ammonia (blank). Note that the signal at the *m/z*: 814.9 – in this blank spectrum – does not completely overlap with the signal at the *m/z*: 815.5 – recorded when analyzing the sample of *Closterium acerosum* cells (cf. **Figure 2.12**)..... 28
- Figure 2.14** MALDI-MS/MS spectra of the three ions corresponding to the MALDI images depicted in **Figures 2.12** and **2.15**: (A) *m/z* 709.4, (B) *m/z* 779.5, (C) *m/z* 815.5. Precursor ions are marked with asterisks (*). The traces in the left-side column represent full *m/z*-range spectra whereas the traces in the right-side column display the low-*m/z* range (within the same spectra). The tandem mass spectra were obtained from the samples of *Closterium acerosum* (co-crystallized with 9-AA) in the negative-ion mode, using the laser-induced fragmentation technology (LIFT)..... 29
- Figure 2.15** Optical and fluorescence micrographs (top) as well as mass spectrometric images of a single cell of *Closterium acerosum* (bottom). The fluorescence micrograph ($\lambda_{\text{ex}} = 330\text{-}380$ nm) shows the presence of SiO₂/9-AA nanoparticles (yellow color) on the cell surface (before the exposure to gaseous ammonia). MS images were obtained in the negative-ion mode by MALDI-TOF-MS. Laser beam wavelength: 355 nm; frequency: 50 Hz; diameter: 10 μm ; raster spacing: 10 μm . Scale bars: 200 μm 31

Figure 2.16	MALDI-MS imaging of small cell ensembles using <i>Anabaena</i> sp. as a model. Optical and fluorescence micrographs (top) obtained using two different excitation wavelengths ($\lambda_{\text{ex}} = 510\text{-}560$ and $330\text{-}380$ nm – middle and right, respectively) and MALDI-MS images of <i>Anabaena</i> sp. (bottom) after the treatment with $\text{SiO}_2/9\text{-AA}$ nanoparticles and ammonia vapors. The MS images were obtained in the negative-ion mode by MALDI-TOF-MS. Laser beam wavelength: 355 nm; frequency: 50 Hz; diameter: 10 μm ; raster spacing: 10 μm . The red-color dashed line in approximately delimits the MS imaging area. Scale bars: 100 μm	32
Figure 3.1	Multi-point multi-wavelength flow-through optical detector. (A) Assembly of the device. (B) Absorbance measurement in an individual channel. Note that only up to 3 channels were used in this study.....	37
Figure 3.2	The design of the Y-junction used to generate segmented flow.....	39
Figure 3.3	Measurement of the effective flow rate in the fused silica capillary used as ESI emitter. (A) The ESI emitter is installed in the flow line, and the MS is on. (B) The ESI emitter is taken away, and adhesive tape is used to prevent leakage of the liquid medium through the small hole made in the wall of the Tygon tubing.....	41
Figure 3.4	Recording convection with segmented and continuous flow. (A) Experimental setup used in the real-time sampling with/without segmented flow prior to detection by the flow-through optical detector (<i>cf.</i> Figure 3.1). The segmented flow was generated by pushing <i>n</i> -octanol towards the Y-junction while the bulk of the liquid was withdrawn by a syringe pump at the outlet of the flow line.....	42

- Figure 3.5** Photograph of the vial (nominal volume: 20 mL) during the convective mixing of 100 μL ferroin with 15 mL water (aided by heating). The ID of capillary used for on-line sampling was 320 μm 43
- Figure 3.6** Convective mixing of ferroin with water followed by segmented flow and flow-through optical detector (*cf.* **Figure 3.1**; wavelength: 518 nm). The red line represents the original data while the blue line shows the final data extracted by the custom software. The two traces were shifted vertically for clarity..... 44
- Figure 3.7** Recording convection with segmented and continuous flow. (A) The output data (red line) obtained with the segmented flow sampling (2 replicates). The blue dashed lines correspond to the exponential functions fitted to the experimental data (after removal of *n*-octanol-related features from the trace): a: $f(t) = 31 \times (1 - e^{(-0.003t)})$; b: $f(t) = 52 \times (1 - e^{(-0.003t)})$. The features marked with asterisks (*) are due to air bubbles. (B) The output data (red line) obtained with the continuous flow sampling (2 replicates). The blue dashed lines correspond to the exponential functions fitted to the raw data: a: $f(t) = 27 \times (1 - e^{(-0.003t)})$; b: $f(t) = 43 \times (1 - e^{(-0.003t)})$ 45
- Figure 3.8** An alternative representation of the data sets displayed in **Figure 3.7A** and **3.7B** (upper graphs). The experimental data points were subtracted with the fitted exponential functions (A: $f_1(t) = 31 \times (1 - e^{(-0.003x)})$; B: $f_2(t) = 27 \times (1 - e^{(-0.003x)})$). Fluctuations of absorbance due to convection currents in the glass vial can be clearly seen..... 46

- Figure 3.9** Sequential convection of two substances with different visible light absorption maxima. (A) Photographs of the vial (nominal volume: 20 mL) filled with 15 mL of water after injection of blue ink (three pictures to the left), and ferroin (three pictures to the right). (B,C) Sampling and detection of the vial content by segmented-flow used in conjunction with the home-made optical detector (*cf.* **Figure 3.1**). (B) Measurement started after the injection of 100 μL of blue ink (50 \times diluted original sample). (C) Measurement started after subsequent addition of 100 μL of ferroin sample. The delay time between red/green and green/blue channels is ~ 2.5 s. The raw data have been treated with a custom software in order to eliminate the peaks due to the *n*-octanol plugs. Traces were shifted vertically for clarity..... 48
- Figure 3.10** UV/Vis absorption spectra of (A) ferroin (2.8×10^{-5} M), and (B) blue ink (1000 \times diluted original solution)..... 49
- Figure 3.11** Application of the hyphenated system – incorporating the home-made optical detector (*cf.* **Figure 3.1**) and mass spectrometer – in the monitoring of the chemical current due to convection. Nominal volume of the vial volume of the vial is 20 mL. The vial was completely filled with ~ 21 mL the aqueous medium containing the internal standard (caffeine)... 49

Figure 3.12 (A,B) Measurement of the relative changes in the concentration of ferriin in the course of convection. (A) Optical detection; the raw data (red line) were fitted with an exponential function ($f(t) = 31 \times (1 - e^{(-0.0035t)})$, blue line). (B) MS detection; the smoothed data were fitted with an exponential function ($f(t) = 7.5 \times (1 - e^{(-0.0030t)})$, blue line). The data acquisition with MS started 132 s after the start of the data acquisition with the optical detector in order to compensate for the dead-volume delay..... 51



Acknowledgements

真的好不敢相信！被苦其心智了兩年，終於輪到我畢業了！每每次經過新竹北上交流道的入口，真的好想衝上去、給他回家算了，但因為火候不夠，只能就此作罷；現在被赦出頭，終於拿到衝上北上交流道且一去不復返的資格，準備迎接我的人生第七春。這一路辛苦下來，要感謝的人真的比我的頭髮還多(我對我頭髮數量相當自豪)；首先是要謝謝我的指導教授帕偉鄂本老師，他跟馬可波羅一樣橫跨了歐亞大陸來台當我的恩師，對我的實驗、英文和生活方面上真的給我不少的幫助；也感謝陳月枝老師提供我實驗上的各種幫忙，能讓我的名字出現在數篇 paper 的作者欄上面。接著感謝實驗室同屆的壯士們(以下照筆畫順序排列)：辛苦扛了一年大總管的大包、研所最後日子的好室友肉圓、同樣被調職的金桔和很愛遊戲王的 Rota。再來也要感謝(以下順序隨機排列)：四位訓練我的啟蒙學長姊大叔、采蓉、喳喳和韓三，能把我實驗技能的底子帶上來；也謝謝曾經一人扛起實驗室的巴斯還有張大哥、在細胞室幫我上課的家樺學長、在我碩一下加入愛跳舞的小禿、一樣在我碩一下進來且同樣被調職的傑筆，還有實驗室之後的新血們：翁小姐的好麻吉書玄、GSH 真的辛苦了的煒茹、同樣來自埔里的丁煦、以後激戰 2 的戰友凱達、白癡白癡的英鈞、交大地主膝哥、食量超大的量承、頭髮超酷的學長和斯里蘭卡來的馬蒂，就因為有這群實驗室的好伙伴，我才能被置之死地然後順利後生！當然也要感謝我的家人們，放家能回家跟爸媽你們聊天真的很開心，還有買了 PS3 的大哥，我回家後就要跟你搶電動了！再來是快不新鮮的大學新鮮人妹子和內心比外表「成熟」的柏頓，有了你們我才能好好享受放假回家的愉快生活；而遠從高雄趕來參加我畢業點禮的奕坦，真的太謝謝妳大老遠來找我和幫我拍碩士服照！也要感謝大學以來的好友們：富為(在研所孽緣斷不了又當了兩年室友)、登山一哥紅芭樂、愛死橋牌的興遠、愈來愈宋慧喬的美人、頭髮比我捲的老二、王牌業務阿碩、打仗要靠你了的黑人和小吳的新員工鴨子，放假能跟你們吃飯聊天真的是我碩所最開心的日子之一。一定要感謝聽我抱怨很多研所的慘事的小綠，也祝賀妳最後成功達到目標。接著還有發福很多的玄維、順利催毀魔戒並回到夏爾的小潘、當初帶我入門二胡的色長旻傑、在中研院奮鬥的妙妙、在原分所辛苦做實驗的大雯、國中同學跟研所同校的國峯、高中同學研所也同校的偉振，感謝你們在我這兩年生活的陪伴；還有感謝系辦幫忙我很多的明君、淑芬和小阿姨小姐們；最後也要感謝這兩年很照顧的我長輩們：中央 TEM 第一把腳椅翁小姐、清夜的果汁阿姨和蔥抓餅阿姨、博愛校區那的饅頭肉排蛋老闆娘、看到我會自動拿大餅和水煎包的素食老闆還有前交大素食部的老闆等等等。沒事再順便感謝一下陪我渡過口試前一天的蝙蝠俠、吸血鬼和狼人們。我能順利念完研所，要感謝的人真的是太多了，沒有你們我真的不知能不能撐下去，總之，謝謝謝謝謝謝謝謝大家！！感謝國科會提供實驗經費和國立交通大學幫助添購 ESI-MS 讓我能順利完成研究。

Chapter 1

Introduction

1.1. Foreword

In many studies related to chemistry, biology, or medicine, it is necessary to investigate chemical composition of complex samples. For this reason, it is not surprising that hundreds of analytical instruments and methods have been developed over the past two centuries; they are based on various concepts, including chromatography, optical spectroscopy, electrochemistry, as well as mass spectrometry (MS). Using these analytical platforms, one can nowadays identify and quantify a large variety of analytes.

During the last decade, spatial and temporal resolutions have become increasingly important features of analytical techniques. For example, using matrix-assisted laser desorption/ionization (MALDI)-MS imaging, one can study distributions of chemical molecules on sample surfaces. Such analyses can provide high-quality molecular images. Nowadays efforts are made to increase the spatial resolution in molecular imaging, and thus provide the possibility of mapping chemical compositions of biological samples on the microscopic level.

Chemical analysis performed in real time is also an important topic in modern chemistry. High temporal resolution is a significant “added value” in the analytical measurements. One way to preserve temporal resolution is to digitize bulk samples collected from the environment by aliquoting them into micro- or sub-micro-liter volume segments. This can prevent longitudinal diffusion and dispersion of the digitized solutions along the flow line. In

fact, segmented-flow systems have widely been used in analytical chemistry, and this approach is very promising for coupling dynamic chemical systems with various detection techniques.

1.2. Matrix-assisted laser desorption/ionization mass spectrometry

1.2.1. Principles of matrix-assisted laser desorption/ionization

The matrix-assisted laser desorption/ionization is a technique which enables desorption of analytes adsorbed on flat conductive targets, and simultaneous ionization in the gas phase prior to separation in the mass analyzer.¹ The original concept of MALDI was demonstrated by Dr Franz Hillenkamp.² In the course of sample preparation for MALDI-MS, samples are typically mixed and co-crystallized with a chemical matrix, which can absorb the ultraviolet (UV) laser light (**Figure 1.1**). The most common wavelengths used for this purpose are 337 nm (nitrogen laser) and 355 nm (Nd-YAG laser). When the UV laser light impinges onto the crystalline deposit of the MALDI matrix with the sample, the ionization (*e.g.* protonation, deprotonation) of analyte molecules may occur. The gas-phase ions are then injected to the mass analyzer in order to determine their mass-to-charge (m/z) ratios. MALDI-MS has widely been used in the analysis of small organic molecules, peptides, proteins and synthetic polymers.¹

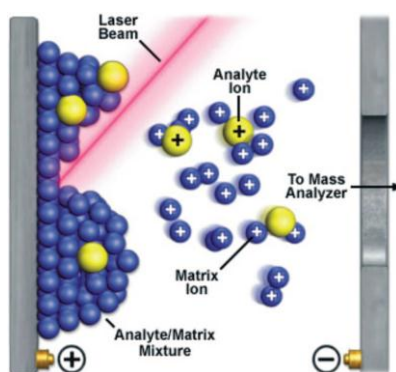


Figure 1.1 The process of desorption/ionization in MALDI. Figure reproduced from reference 3.

1.2.2. MALDI matrix

There are numerous kinds of MALDI matrices. Different matrices are suitable for the ionization of different analyte molecules: for example, in the positive-ion mode, 2,5-dihydroxy benzoic acid (2,5-DHB) is often used in the analysis of peptides^{4,5} while 3,5-dimethoxy-4-hydroxycinnamic acid (sinapinic acid, SA) is used in the analysis of proteins.^{6,7,8} In the negative-ion mode, 9-aminoacridine (9-AA) is often used in the analysis of nucleotides and lipids^{9,10,11} When the solvent of the matrix/sample mixture evaporates, a crystalline deposit remains on the sample plate. The crystallization pattern is usually far from homogeneous. This contributes to the so-called “sweet-spot effect”;¹² due to the heterogeneous/chaotic crystallization of the matrix and the analytes, some locations of the MALDI spots give rise to high signals while the other locations mostly contribute to the spectral noise. In the conventional qualitative use of MALDI-MS, the “sweet-spot effect” does not affect the results to a great extent because one can still record high-quality spectra, and identify the molecules producing peaks with satisfactory signal-to-noise (*S/N*) ratios. However, in the case of MALDI imaging, the “sweet-spot effect” may significantly deteriorate the quality of the MS images, decrease the spatial (lateral) resolution, and contribute to artifacts. When using inorganic particles or surfaces as matrices in the so-called “surface-assisted laser desorption/ionization mass spectrometry (SALDI-MS)”,¹³ the problem of heterogeneous crystallization is mitigated.¹⁴

1.2.3. Time-of-flight mass analyzer

Time-of-flight (TOF) is the most common mass analyzer used in MALDI-MS.¹⁵ The gas-phase ions are accelerated in an electric field, and shifted to the TOF tube. As the ions move in the TOF tube, all of the them have the same kinetic energy but different velocities. The analyte ions with smaller *m/z* will move faster and reach the detector first, while the ions with higher *m/z* will reach the detector later. Finally, the *m/z* values can be calculated based

on the time elapsed during the migration of the ions from the source to the detector.

1.2.4. MALDI imaging

One of the important applications of MALDI-MS is MALDI imaging. In fact, MALDI imaging has widely been used to investigate chemical distributions of lipids, proteins, and small molecules, within biological specimens.¹⁶⁻²⁰ In order to obtain a MALDI image, the UV laser beam needs to be raster-scanned over the sample surface (pre-coated with a MALDI matrix), spectra recorded at each of the sampling positions and then converted to molecular images of the sample surface (for an example, see **Figure 1.2**). Usually this is done by plotting the intensities of the selected peaks (often following a normalization step) as two-dimensional maps, in which the saturation level corresponds to the signal intensity.

As pointed out above, sample preparation is crucial for achieving high spatial resolution in MALDI imaging. In particular, it is very important that the whole sample surface is evenly coated with the MALDI matrix. Several methods have been proposed for coating specimens with MALDI matrices, and some of them can provide relatively high spatial resolutions; they include coating with a pneumatic spray, electrospray deposition (for reviews, see refs 16, 17, 21), and matrix sublimation/recrystallization method.²²⁻²⁴ In this work, we demonstrate a new type of matrix coating method, which takes advantage of hybrid nanoparticles (used as a matrix carrier) in order to record MALDI images of single cells.

1.3. Electrospray ionization mass spectrometry

1.3.1. Principles of electrospray ionization

The electrospray ionization (ESI) is an atmospheric pressure ionization method, used to produce gas-phase ions, which are subsequently analyzed by mass spectrometry. This ingenious approach was developed by Dr. John Fenn. In this technique,³⁵ the samples are delivered in liquid phase, typically dissolved in water or organic solvents (*e.g.* acetonitrile or

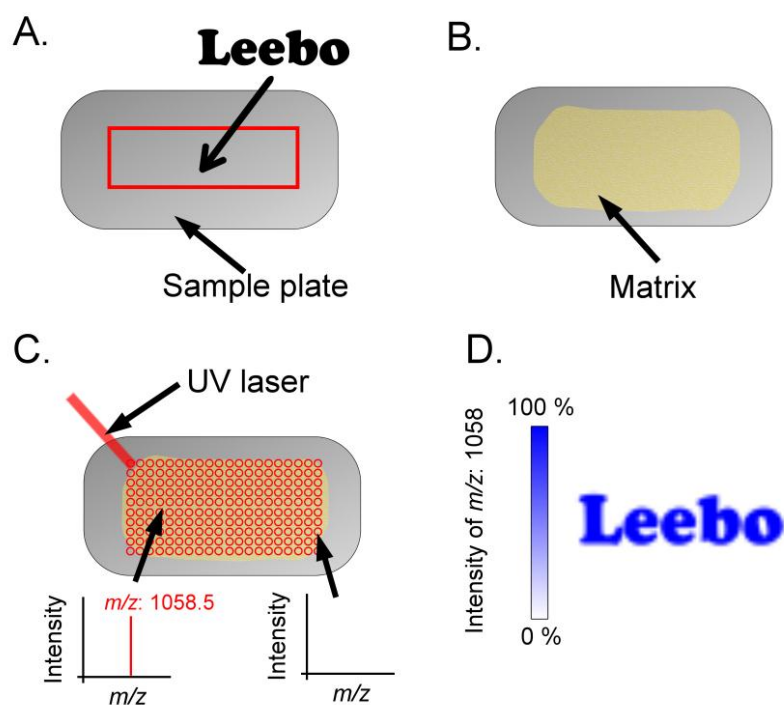


Figure 1.2 The principle of MALDI imaging. (A) A sample containing bradykinin acetate ($[M+H]^+$ at m/z 1058.5) is used to write “Leebo” on a MALDI sample plate. (B) Matrix is coated on top of the sample plate. (C) UV laser beam is raster-scanned over the sample. The sampling sites are indicated with red circles. If a site illuminated by the laser beam contains bradykinin acetate, a signal at the m/z 1058.5 (in the positive-ion mode) will be recorded. (D) The spectra collected in (C) are converted to a molecular map depicting the distribution of bradykinin on the plate surface.

methanol). A common way to apply samples is by using syringe pump connected to a capillary emitter mounted at the outlet of the flow line. For the electrospray process, it is also necessary to apply a potential difference between the electrospray emitter and a counterelectrode (typically the orifice of the mass spectrometer, **Figure 1.3**). The Taylor cone and jets are then formed at the outlet of the emitter, which is followed by the detachment of charged microdroplets.³⁶ Desolvation of the microdroplets takes place as they advance towards the inlet of the mass spectrometer. When the so-called “Rayleigh limit” is reached,

the Coulombic repulsion force is higher than the surface tension within a droplet, and the droplet splits into smaller ones.³⁶ Combined with continuous evaporation of the solvent, this process will eventually lead to the formation of singly or multiply charged analyte species in the gas phase. The mass-to-charge ratios (m/z) are subsequently determined in the mass analyzer.

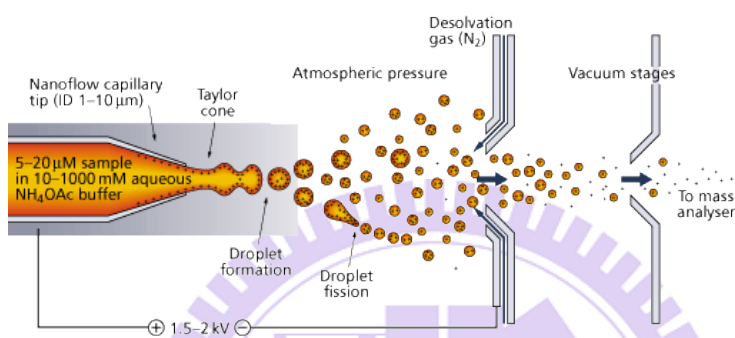


Figure 1.3 The process of electro-spray ionization. Figure reproduced from reference 37.

One of the advantages of ESI is that it is straightforward to obtain multiply charged species. This property is very convenient for the analysis of proteins and other high-molecular-weight molecules (> 4000 Da). The common mass analyzer (*e.g.* ion trap, quadrupole) have a relatively low m/z limit 4000 Da; however, the multiply charged biomolecules with high molecular weight may still fall within the operational m/z range of the mass spectrometer.³⁸ It is also very convenient to couple the ESI-MS instruments with different types of separation systems. For example, it is quite common to hyphenate liquid chromatography (LC)³⁹ or capillary electrophoresis (CE)⁴⁰ with ESI-MS in order to perform on-line analysis.

1.3.2. Ion-trap mass analyzer

The ion trap is a mass analyzer which can trap the ions within a three-dimensional space. It commonly incorporates a ring electrode and two metal end-cap electrodes (**Figure 1.4**).

When the analyte ions enter the ion trap, a radio-frequency (RF) and direct current (DC) voltage applied to the electrode, contribute to trapping the ions with specific m/z , which at certain conditions will move along a stable orbit. After gas-phase ions are trapped in the analyzer, they can be ejected to the detector by increasing the amplitude of RF voltage applied to the ring electrode (stability limit ejection method), or end caps (resonant ejection method). It will cause the ions with a specific m/z leave the trapping region from the z direction (**Figure 1.4**), and move towards the detector.⁴²

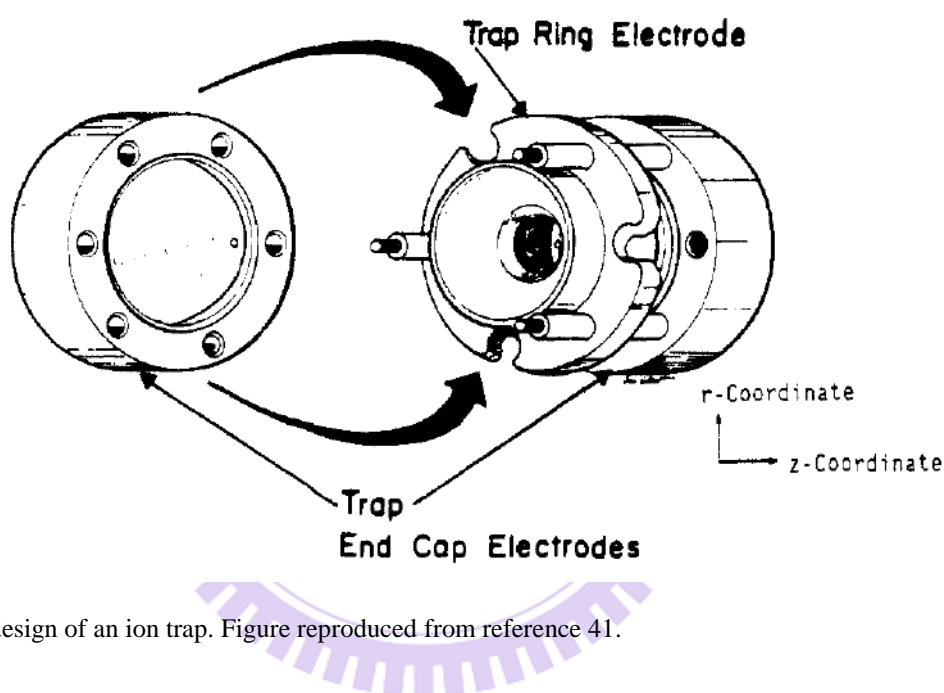


Figure 1.4 The design of an ion trap. Figure reproduced from reference 41.

1.4. Optical absorption detection

When a light beam impinges on a semi-transparent sample, some of the light is absorbed. For example, if a solution has red color, it absorbs light in the wavelength range $\sim 380\text{-}560$ nm, while red light ($\sim 590\text{-}740$ nm) will be transmitted or reflected from such sample. This simple example gives a reason why many liquid solutions in our surrounding have a color. The phenomenon of the absorption of light is described by the absorption laws outlined below.

When a light beam with the intensity P_0 is shone onto a liquid sample, a fraction of photons will be absorbed but some light will be transmitted (**Figure 1.5**). If we denote the intensity of the transmitted light as P_1 , we can then define the value of transmittance (T) as the ratio:

$$T = P_1/P_0 \quad (1)$$

The transmittance can readily be converted to absorbance (A) by using the logarithmic expression:

$$A = -\log T = \log (P_0/P_1) \quad (2)$$

The higher the absorbance, the less light has been transmitted through the sample. Since the measured absorbance is affected by the optical pathlength, and the concentration of the analyte, the following expression is valid:

$$A = \varepsilon b c \quad (3)$$

where b is the optical pathlength, c is the concentration of the analyte solution and ε is the molar absorptivity. The equation 3 is referred to as the Beer-Lambert law (or Beer's law).²⁵ From the equation 3 it is clear that an increase of the optical pathlength (b), as well as the concentration of the analyte (c), will be accompanied by an increase of the absorption of light within the sample of the solution under analysis. The Beer-Lambert law has widely been used in quantitative analysis. Since the absorption of light is directly related to the concentration of an analyte, we can fix the optical pathlength (*i.e.* use the same vial/cuvette), and measure absorbances of samples with different concentrations of this analyte.

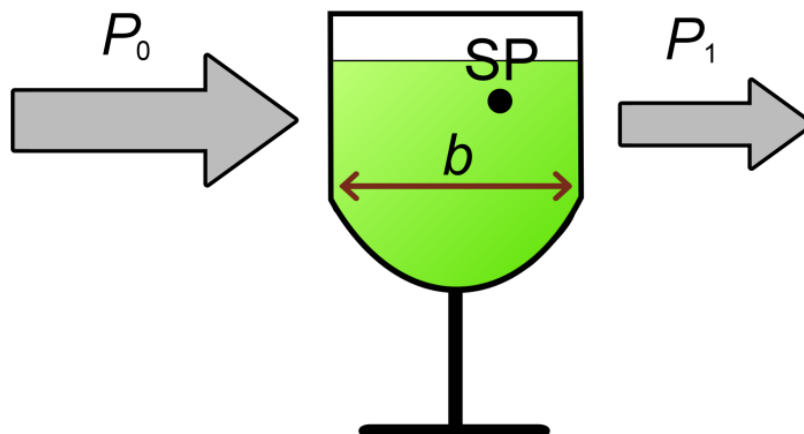


Figure 1.5 The incident light (P_0) passes through a sample; the light beam intensity after the optical cell is lower than that of the incident light beam ($P_1 < P_0$) which shows that the sample is not completely transparent to light at the wavelength used. The length b is the optical pathlength. The point SP is a “sampling point” (see section 1.5)

1.5. Segmented flow

It should be pointed out that the optical absorption spectroscopy, characterized by equations 1-3 is generally applied to homogeneous solutions. If a solution is not homogeneous, applying the detection strategy depicted in **Figure 1.5** will give us information on the average absorbance of the sample along the illumination axis. If one wants to measure the absorbance at one location of a three-dimensional vessel (for example, point SP in **Figure 1.5**), an alternative detection strategy has to be implemented.

A very simple way to obtain such information — which is further elaborated in chapter 3 — would be to probe the contents of the sample vessel into a thin tubing (*e.g.* capillary), and subsequently transfer the collected samples to a detector. This method allows one to collect samples at a given point of the three-dimensional space (*e.g.* point SP in **Figure 1.5**), and measure the absorbance of the medium in the corresponding microenvironment. However,

transferring samples along capillaries (from the inlet towards the detector) by hydrodynamic flow can contribute to significant dispersion (**Figure 1.6**), and this way decrease the temporal resolution and sensitivity of the measurement.

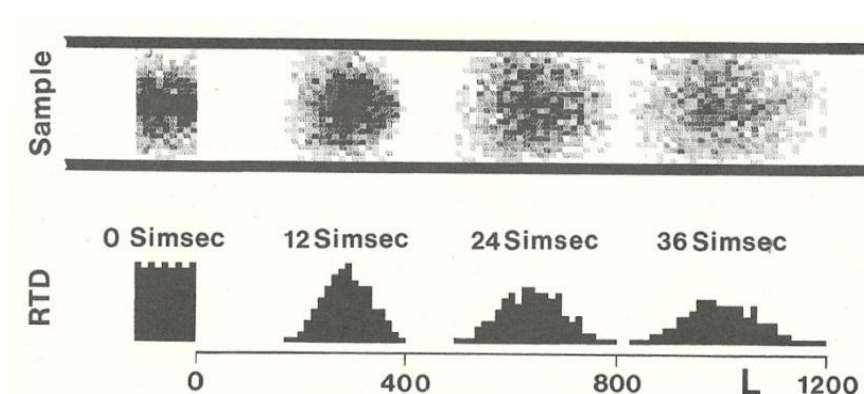


Figure 1.6 Dispersion of a sample plug in the continuous (hydrodynamic) flow. Figure reproduced from reference 26.

In order to prevent the dispersion (due to advection and diffusion), and this way increase the temporal resolution of sampling detection, the segmented-flow approach can be implemented. Segmented flow can easily be generated by simultaneous injection of two immiscible fluids (two liquids or liquid/gas) into a capillary or a microfluidic channel (**Figure 1.7**).²⁷⁻²⁹ Mixing occurs mainly within the samples encapsulated in each droplet (**Figure 1.8**), while the longitudinal dispersion/diffusion and carry-over effect are reduced.^{30,31}

After the sampling, the plugs can readily be transported towards the optical absorption detector, and the Beer-Lambert law can be used to determine the absorbance of each droplet collected at point SP (*cf.* **Figure 1.5**). This sampling method may potentially enhance the temporal resolution of analysis conducted by optical absorption detection, and other platforms.³²⁻³⁴

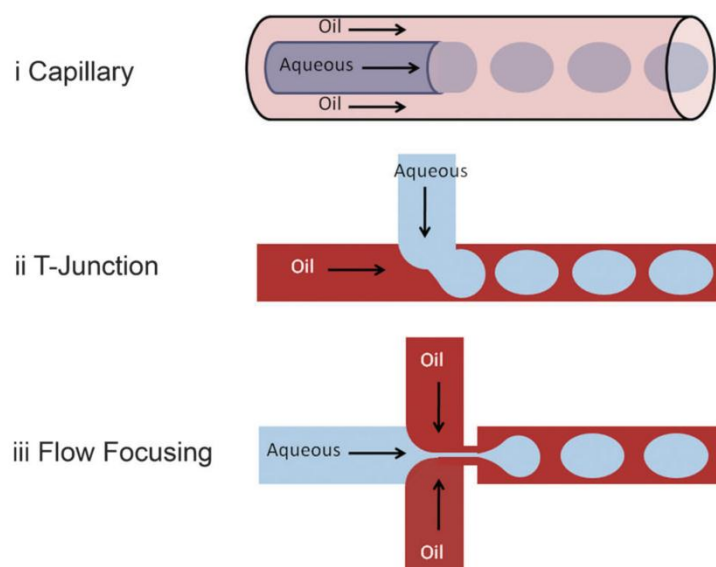


Figure 1.7 Methods for producing segmented flow. Figure reproduced from reference 29.

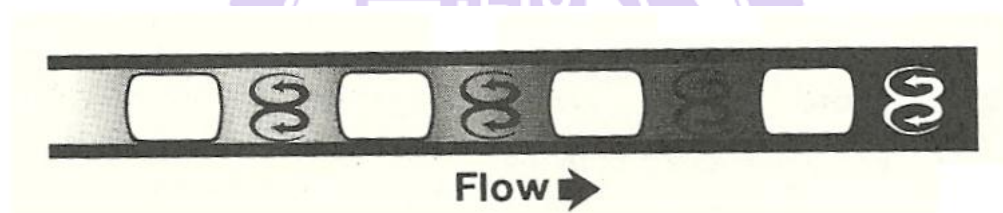


Figure 1.8 Separation of individual segments of samples (grey to black) with air bubbles (white) along the flow line; mixing of the transported liquid within the segments (arrows). Figure reproduced from reference 30.

1.6. Goals of the work

In this work, we were aiming to develop two analytical methods, one preserving spatial resolution, and the other one preserving temporal resolution.

- The goal of the first study was to develop a new type of MALDI matrix, based on hybrid nanoparticulates, which would enable performing MALDI imaging of single cells at a high spatial resolution.

- The goal of the second study was to develop a method useful in the monitoring of heterogeneous dynamic chemical systems while preserving temporal resolution. The method should accommodate optical as well as mass spectrometric detection.



Chapter 2

Hybrid nanoparticles for mass spectrometric imaging of single cells

2.1. Introduction

As outlined in section 1.2, Matrix-assisted laser desorption/ionization (MALDI) is an analytical technique in which laser light is used to desorb and ionize molecules – previously co-crystallized with a chemical matrix – to enable mass spectrometric (MS) detection of the resulting gas-phase ions.^{1,2} One of the interesting features of this technique is the possibility of mapping chemical distributions of analytes in biological specimens. In fact, MALDI-MS has widely been used for mapping lipids,⁴³⁻⁴⁵ proteins,⁴⁶⁻⁴⁸ and small molecules⁴⁹⁻⁵¹ in the samples such as tissues or single cells.^{17,20,23,52-54} Examples of powerful chemical matrices used in MALDI include α -cyano-4-hydroxycinnamic acid (CHCA), 2,5-dihydroxybenzoic acid (2,5-DHB), and 9-aminoacridine (9-AA). Before analysis, concentrated solution of a selected chemical matrix is applied onto the surface of the biological sample. The biggest nuisance in MALDI imaging is the heterogeneous crystallization of MALDI matrices on the sample surface, which considerably decreases lateral resolution of the resulting images, and often disables the possibility of performing single-cell studies. Homogeneous and reproducible application of MALDI matrices is critical for obtaining high-quality results using this technique.

Here we demonstrate a new type of hybrid inorganic-organic nanomaterial which enables *in-situ* delivery of a chemical matrix for mass spectrometric imaging with high lateral

resolution. Application of the hybrid matrix to biological specimens poses less threat to the experimenters and the environment since the toxic matrix compound does not need to be sprayed by using a gas-powered sprayer, which could lead to the contamination of the laboratory environment with toxic aerosols. The hybrid nanomaterial binds to the surface of the cells while still in the liquid phase, which is followed by a controlled release of the organic matrix molecules triggered by alkaline vapors delivered to the specimen in a closed chamber.

2.2. Materials and methods

2.2.1. Materials

Acetyl coenzyme A, adenosine triphosphate, 9-aminoacridine (9-AA), ammonium hydroxide (33% solution), bradykinin acetate, guanosine triphosphate, tetraethoxysilane (TEOS), and uridine diphosphate glucose were purchased from Sigma-Aldrich (St. Louis, USA). 1,2-Dipalmitoyl-*sn*-glycero-3-[phospho-*rac*-1-glycerol] was purchased from Avanti Polar Lipids (Alabaster, USA). Ethanol was purchased from Echo Chemical (Miaoli, Taiwan). Water (18.2 M Ω ·cm at 25 °C) was obtained from a Milli-Q water purification system (Merck Millipore, Billerica, USA). Indium tin oxide (ITO) glass slides were purchased from Bruker Daltonics (Part No. 237001; Bremen, Germany). Aluminum plate (thickness: 200 μ m) was obtained from a local supplier and cut into small pieces in house.

2.2.2. Synthesis of SiO₂/9-AA and SiO₂ nanoparticles

In order to synthesize SiO₂/9-AA nanoparticles, 54.4 mg of 9-AA and 97 μ L of 33% NH₃(aq) solution were mixed with 15.25 mL 50% ethanol solution (**Figure 2.1**). The mixture was sonicated until almost all 9-AA crystals were dissolved, and saturation of the solution with 9-AA was reached. The mixture was further stirred for 30 min, and 117.3 μ L of TEOS were subsequently added. Stirring continued for 5 min, and the suspension was then left to

settle for 12 h. The color of the resulting suspension was bright-yellow. The as-prepared SiO₂/9-AA nanoparticle suspension was centrifuged (5500 rpm, 20 min). The SiO₂/9-AA nanoparticles were recovered from the pellet, and they were rinsed with 50% ethanol. After that, they were resuspended in water and stored in the refrigerator at 4 °C.

To synthesize SiO₂ nanoparticles (without 9-AA), 3 mL of 30% ammonia solution were mixed with 7.63 mL 99.5% ethanol and 6.13 mL water. The mixture was further stirred for 30 min, and 117.3 μL of TEOS were added. Stirring continued for 5 min, and the product suspension was left to settle for 12 h. The as-prepared SiO₂ nanoparticle suspension was centrifuged (5500 rpm, 20 min), followed by rinsing the nanoparticles with 50% ethanol. The SiO₂ nanoparticles were also resuspended in water and stored in the refrigerator at 4 °C. Samples of SiO₂/9-AA and SiO₂ nanoparticles were analyzed using a scanning electron microscope (SEM; JEOL JSM-7401 F, Tokyo, Japan).

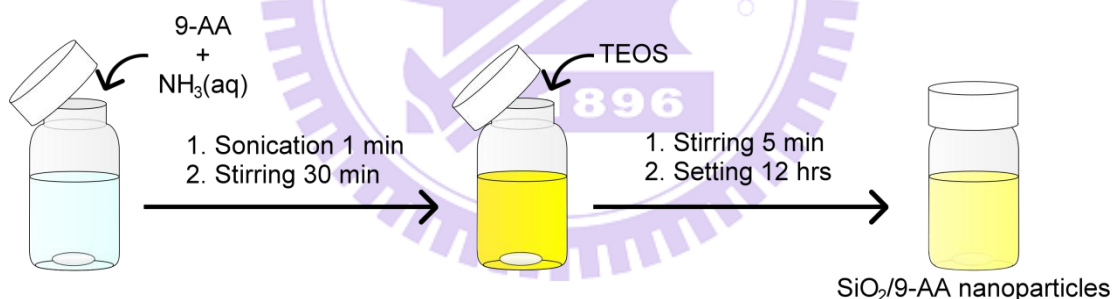


Figure 2.1 Synthesis of the hybrid SiO₂/9-AA nanoparticles.

2.2.3. The controlled release of 9-AA from SiO₂/9-AA nanoparticles by alkali

In order to demonstrate the feasibility of the controlled release of the 9-AA MALDI matrix from the SiO₂/9-AA nanoparticles, 200 μL (an equivalent of 0.5 mg mL⁻¹) of SiO₂/9-AA nanoparticle suspension in 50% ethanol solution was prepared. Subsequently, an aliquot of 10 μL 33% NH₃(aq) was added, and the suspension was stirred for 5 min, and

centrifuged at 10000 rpm for 10 min. The supernatant was diluted 100× with 50% ethanol, and used as a sample to obtain the fluorescence spectra by FluoroMax-3 spectrofluorometer (Horiba Jobin Yvon, Edison, USA). The excitation wavelength was set to 400 nm, and the emission spectrum was recorded in the wavelength range of 410-600 nm.

In another experiment – which was designed to demonstrate the controlled release of MALDI matrix – an aliquot of 200 μL 33% $\text{NH}_3(\text{aq})$ was mixed with 200 μL (an equivalent of 5 mg mL^{-1}) $\text{SiO}_2/9\text{-AA}$ suspension, and stirred for 30 min. An aliquot of 200 μL of 95.5% ethanol was subsequently added to solubilize the 9-AA matrix released from the $\text{SiO}_2/9\text{-AA}$ nanoparticles. The suspension of the residue nanoparticles was then centrifuged at 10000 rpm for 10 min, and the pellet fraction containing nanoparticles (after 9-AA release) was re-suspended in 100 μL of pure water. The suspension was then spotted onto an SEM target, and imaged by SEM.

2.2.4. Preparation of algal cells for analysis

The protocol used to prepare single cells of *Closterium acerosum* (Carolina Biological Supply Company, Burlington, USA) for analysis is outlined in **Figure 2.2**. Initially, 0.5 mL of the cell suspension was mixed with 1.5 mL of water, and the resulting suspension was centrifuged at 2000 rpm for 5 min. The supernatant was removed, and the pellet was resuspended in 100 μL of water. A droplet of the resulting dilute suspension of cells was placed in a Petri dish, and several (~ 5) cells were picked up using a micropipette. Cells were washed several times by subsequent transfers into 2- μL droplets of fresh water. A small amount of the suspension of $\text{SiO}_2/9\text{-AA}$ nanoparticles (2 μL , 5 mg mL^{-1}) was pipetted onto the cells, and the excess suspension of the nanoparticles was quickly removed by pipetting. The unbonded $\text{SiO}_2/9\text{-AA}$ nanoparticles were subsequently washed away with water. Finally, 2 μL of water were used to re-suspend the cells, and transfer them onto an aluminum plate. The optical and fluorescence images were captured using an upright fluorescence microscope

(Eclipse 80i; Nikon, Yokohama, Japan) fitted with a digital camera (DS-R1i; Nikon, Tokyo, Japan). Fluorescence images were obtained using the excitation filters: UV-2A ($\lambda_{\text{ex}} = 330\text{-}380$ nm) and G-2A ($\lambda_{\text{ex}} = 510\text{-}560$ nm)

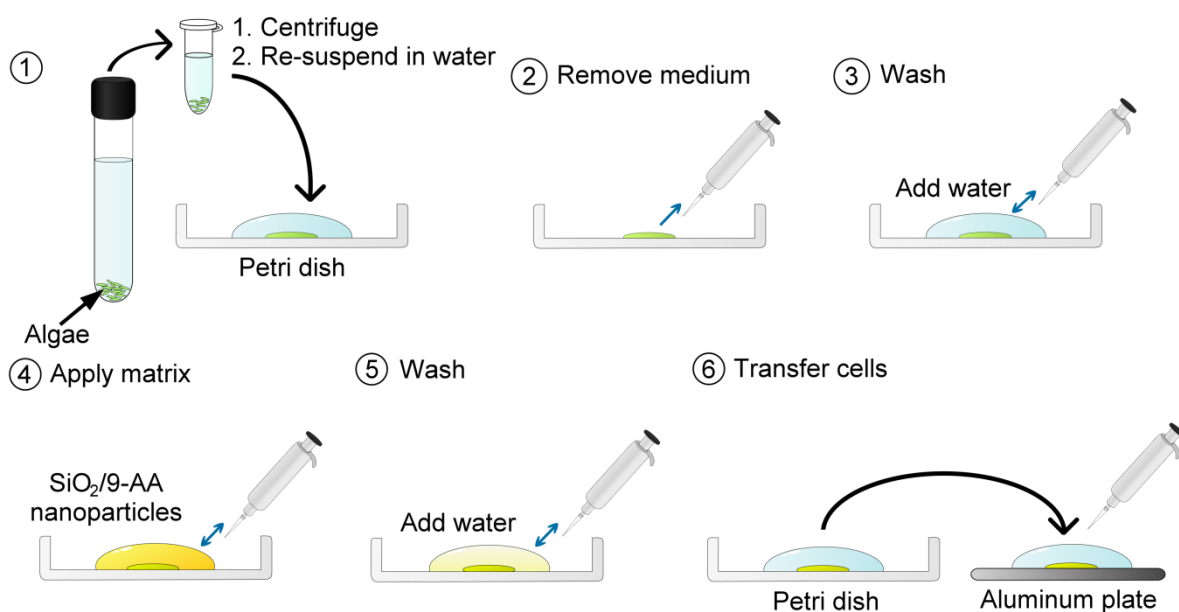


Figure 2.2 Preparation of cells for mass spectrometric imaging.

2.2.5. Controlled release of 9-AA by exposure to ammonia vapors

In order to induce the controlled release of 9-AA from the $\text{SiO}_2/9\text{-AA}$ nanoparticles by exposure to ammonia vapors, a simple incubation system was constructed (**Figure 2.3**). A hole was drilled in the lid of a plastic Petri dish; one side of a silicon tube (length, 40 cm; ID, 2 mm, OD, 4 mm) was slid through that hole, and epoxy glue was used to seal the junction. The other side of the silicon tube was passed through the rubber septum mounted on the top of a 20-mL glass vial acting as the ammonia-vapor generator. The vial was filled with ~15 mL 33% $\text{NH}_3(\text{aq})$ solution and placed in a water bath set to 50 °C. The release of ammonia vapors occurred instantly – as verified by inserting a wet pH-indicator strip into the Petri dish used as

the incubation chamber. An aluminum target with the sample (algal cells pre-coated with the $\text{SiO}_2/9\text{-AA}$ nanoparticles) was incubated inside the Petri dish containing ammonia vapors for 30 min. Parafilm was used to seal the slit in between the top and bottom parts of the Petri dish, thus to prevent possible escape of gaseous ammonia from the system.

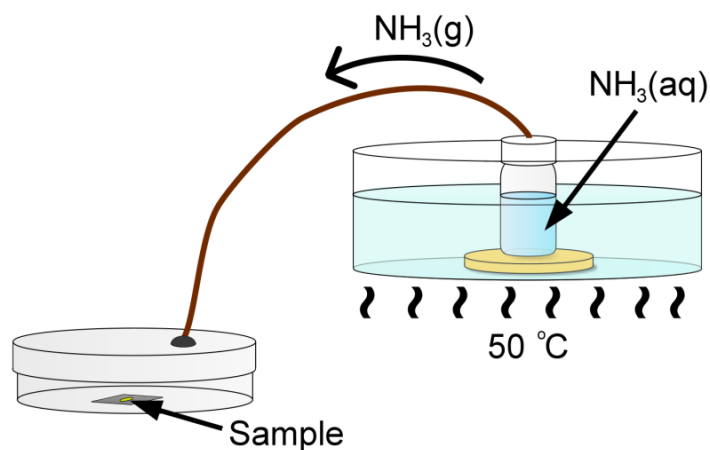


Figure 2.3 Setup for the controlled release of 9-AA in the presence of gaseous ammonia.

2.2.6. MALDI-MS and MALDI imaging

For MALDI-MS detection and MALDI imaging experiments, we used the Autoflex III Smartbeam instrument (Bruker Daltonics) fitted with a solid-state laser ($\lambda = 355$ nm). The settings of this instrument were as follows: negative ion mode, ion source 1, -19 kV; ion source 2, -16.7 kV; lens, -9 kV; delay time, 0 ns. During the MALDI imaging routine, the laser beam was focused to 10 μm , the scan raster was set to 10-15 μm (in different experiments), and 35 laser shots were fired at every raster point at a frequency of 50 Hz. The mass range was set to 300-1100 Da, and a cut-off limit of 300 Da was applied. Data were acquired using the flexControl software (version 3.0; Bruker Daltonics). The MALDI imaging data were collected and viewed using the flexImaging software (version 2.0; Bruker Daltonics).

2.3. Results and discussion

2.3.1. Synthesis and initial testing of the hybrid nanoparticles

It is known that hybrid inorganic-organic materials can be synthesized using the sol-gel reaction system.^{55,56} For example, Laperriere *et al.*⁵⁷ doped 9-AA into glass produced in the course of a sol-gel process. In the present work, we have made an attempt to synthesize SiO₂/9-AA nanoparticles with the prospect of using them as a matrix suitable for high-spatial-resolution MALDI imaging (**Figure 2.1**). To achieve this goal, we substituted a fraction of the alkaline component (NH₃(aq)) of the sol-gel synthesis process with 9-AA. This yielded a suspension of hybrid nanoparticles with the inorganic framework of SiO₂, and the organic filling of 9-AA. **Figure 2.4** presents scanning electron micrographs of the resulting hybrid SiO₂/9-AA nanoparticles as well as SiO₂ nanoparticles (without 9-AA). On the nanoscopic level, the nanoparticles loaded with 9-AA resemble those without 9-AA, however the hybrid nanomaterial has yellow color due to the presence of the 9-AA “cargo”. Since the active MALDI matrix compound (9-AA) is embedded within the inorganic structure of SiO₂, at this stage, the as-prepared hybrid nanomaterial does not yet fulfill the function of MALDI matrix: MALDI-MS detection of four standard compounds mixed with this nanomaterial gave poor results (**Figures 2.5A** and **2.5C**). However, following the release of 9-AA in a chamber saturated with gaseous ammonia (**Figure 2.3**), the recorded MS signals were very high (**Figures 2.5B** and **2.5D**). We have also noticed that – unlike most conventional MALDI matrices – the SiO₂/9-AA nanoparticles form an extremely homogeneous layer on the MALDI target, without almost any signs of heterogeneous crystallization (**Figure 2.6**). This can facilitate application of the matrix by simple incubation of the hybrid nanoparticles suspended in an aqueous solution – compatible with biological specimens.

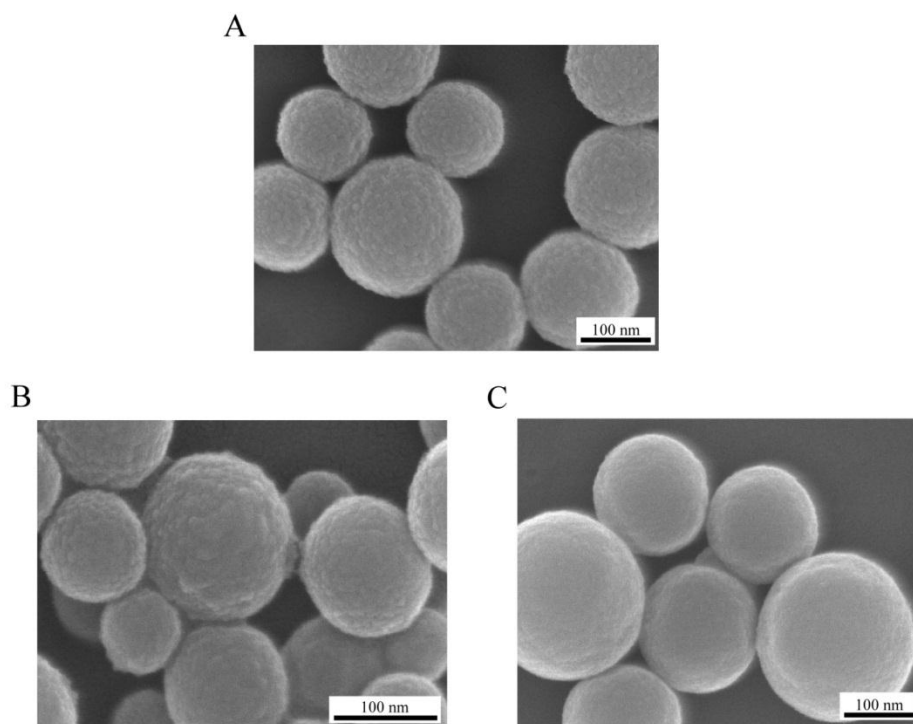


Figure 2.4 Scanning electron micrographs of the hybrid SiO₂/9-AA nanoparticles (A and B) as well as single-component SiO₂ nanoparticles (C and D). (A) SiO₂/9-AA nanoparticles (as synthesized). (B) SiO₂ nanoparticles (without 9-AA) synthesized using 3 mL 33% NH₃(aq). (C) SiO₂ nanoparticles (without 9-AA) synthesized using 4 mL 33% NH₃(aq).

2.3.2. Evaluation of the controlled matrix release process

The controlled release process was further studied in a series of experiments: in one of them, we suspended the SiO₂/9-AA nanoparticles in 50% ethanol, added 33% NH₃(aq), and stirred the resulting suspension for 5 min, centrifuged, and measured the fluorescence of the supernatant (**Figure 2.7A**). Fluorescence intensity of the supernatant decreased in the subsequent washing steps using NH₃(aq) as the washing solvent. In another test, pure water was used instead of NH₃(aq) as the washing solvent; in this case, fluorescence intensity of the supernatant did not decrease as much as when using NH₃(aq) (**Figure 2.7B**). In addition, after the washing with NH₃(aq), the supernatant had yellow color (**Figure 2.7C**). After three

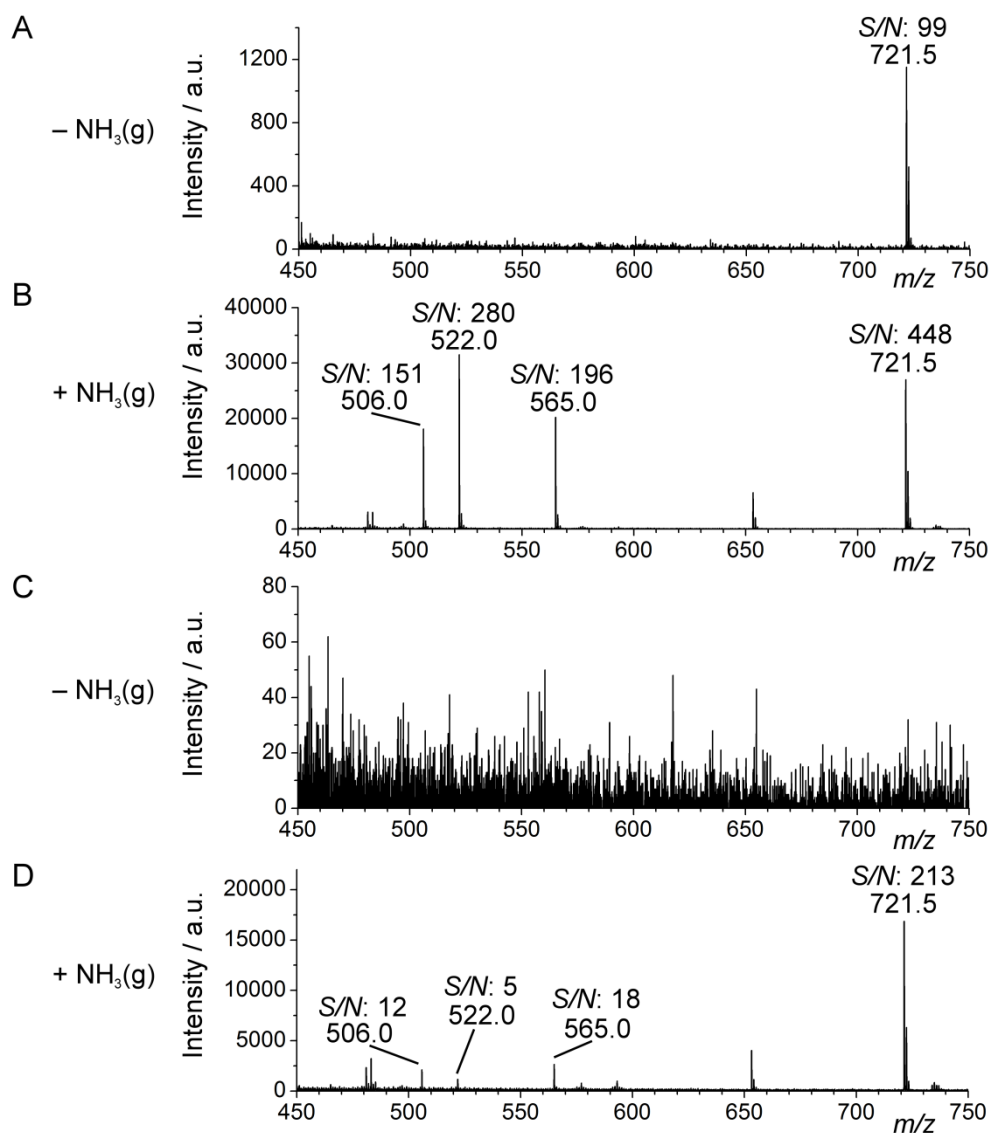


Figure 2.5 The effect of ammonia vapors ($\text{NH}_3(\text{g})$) on signal intensity and signal-to-noise (S/N) ratio in MALDI-MS analysis of a chemical standard solution ($1 \mu\text{L}$) containing adenosine triphosphate (ATP), guanosine triphosphate (GTP), uridine diphosphate glucose (UDP-Glc) and 1,2-dipalmitoyl-*sn*-glycero-3-[phospho-*rac*- α -glycerol] (PG) using $\text{SiO}_2/9\text{-AA}$ nanoparticles as matrix. The sample/nanoparticle deposits in (A) and (C) were not incubated with $\text{NH}_3(\text{g})$ while the sample/nanoparticle deposits in (B) and (D) were incubated with $\text{NH}_3(\text{g})$. Analyte concentrations in (A and B): ATP, GTP, and UDP-Glc – each $2.5 \times 10^{-5} \text{ M}$; PG – $3.6 \times 10^{-5} \text{ M}$. Analyte concentrations in (C and D): ATP, GTP, and UDP-Glc – each $2.5 \times 10^{-6} \text{ M}$; PG – $3.6 \times 10^{-6} \text{ M}$. Peak identities: ATP, m/z 506.0; GTP m/z 522; UDP-Glc, m/z 565; PG, m/z 721.5.

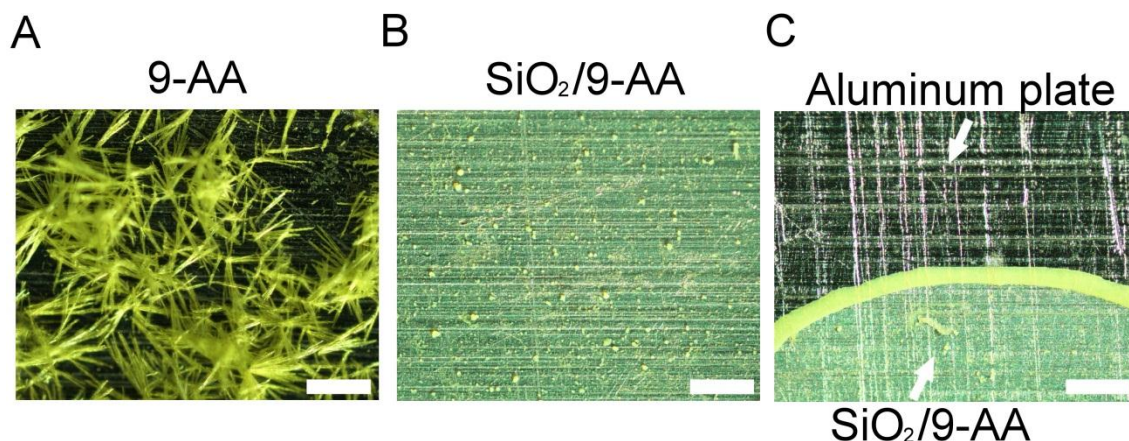


Figure 2.6 Optical micrographs of dry deposits of different samples on an aluminum plate used as MALDI target: (A) 2 μL of 1:1 (v/v) mixture of 9 mg mL^{-1} 9-AA solution in acetone and 10^{-5} M adenosine triphosphate in water; (B) 2 μL 10^{-5} M solution of adenosine triphosphate was allowed to dry, followed by deposition of 0.5 μL suspension of the $\text{SiO}_2/9\text{-AA}$ nanoparticles (5 mg mL^{-1} in water). (C) Micrograph showing the edge of the $\text{SiO}_2/9\text{-AA}$ nanoparticle deposit on the aluminum plate (same as in (B)). Hybrid $\text{SiO}_2/9\text{-AA}$ nanoparticles provide unprecedented homogeneity of the matrix deposit on the microscopic level (B and C), as compared with the heterogeneous crystalline deposit of 9-AA (A). Scale bars: 200 μm .

consecutive wash steps with $\text{NH}_3(\text{aq})$, the supernatant was clear, and the amount of pellet was less than in the control series without $\text{NH}_3(\text{aq})$; this is due to the fact that some of the SiO_2 material got dissolved in the alkaline solution (*cf.* scanning electron micrograph in **Figure 2.8**). These results prove that the structure of the hybrid $\text{SiO}_2/9\text{-AA}$ nanoparticles is degraded in the alkaline environment ($\text{NH}_3(\text{aq})$), and this degradation process is accompanied by the release of 9-AA.

2.3.3. Application in the imaging of single cells

Equipped with the controlled release hybrid $\text{SiO}_2/9\text{-AA}$ nanoparticles, we further aimed to apply this material as a matrix in the mass spectrometric imaging of microscopic specimens such as single cells. As a model sample, we selected unicellular algae – *Closterium acerosum*.

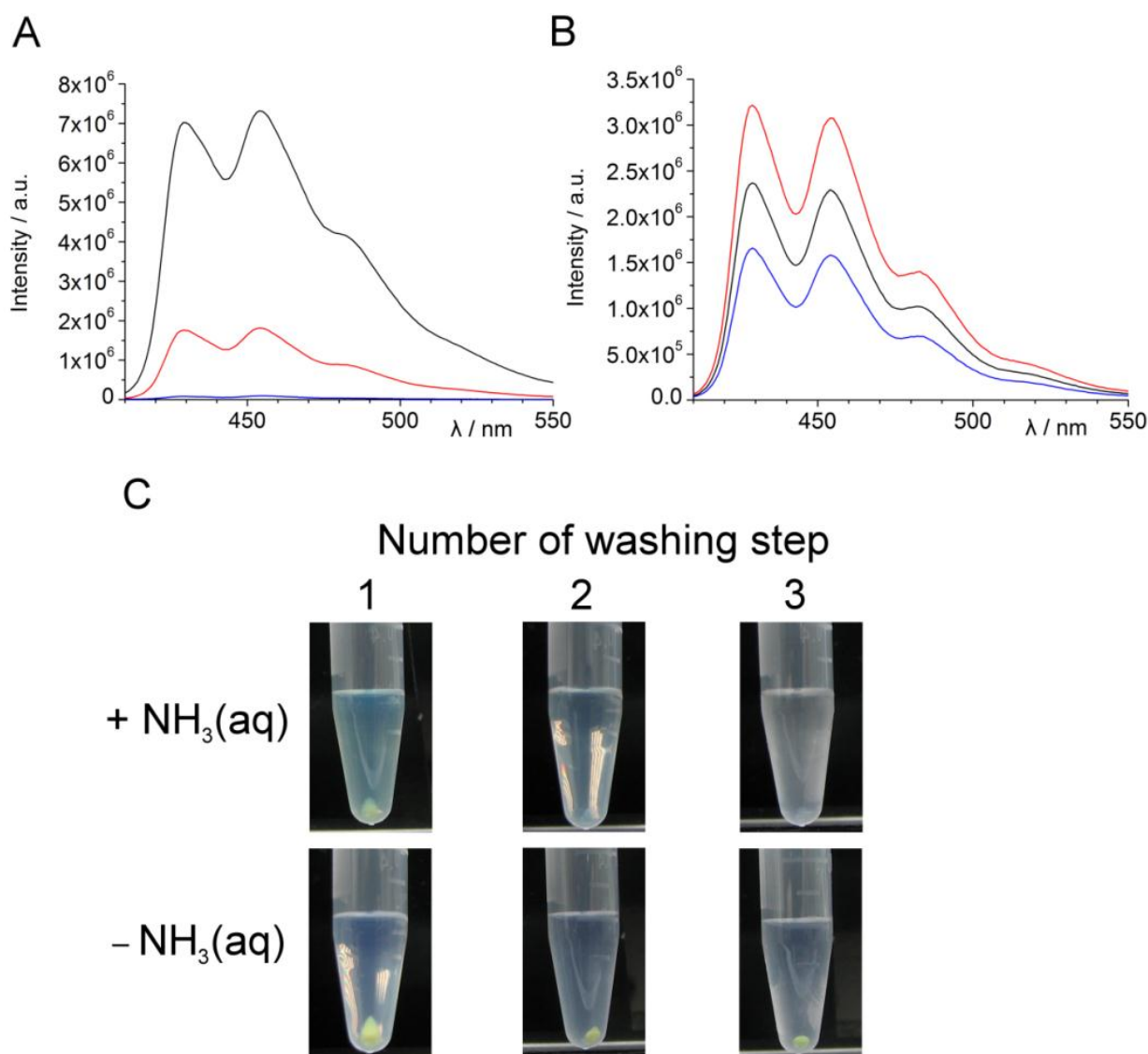


Figure 2.7 Controlled release of 9-AA in the liquid phase. (A and B) Fluorescence spectra ($\lambda_{\text{ex}} = 400 \text{ nm}$) of supernatants collected from the $\text{SiO}_2/9\text{-AA}$ nanoparticle suspensions. (A) Leaching 9-AA from the $\text{SiO}_2/9\text{-AA}$ nanoparticles by addition of $10 \mu\text{L}$ of 33% $\text{NH}_3(\text{aq})$ to $200 \mu\text{L}$ of the 0.5 mg mL^{-1} nanoparticle suspension in 50% ethanol. The pH of the resulting suspension was ~ 14 . (B) Leaching 9-AA from the $\text{SiO}_2/9\text{-AA}$ nanoparticles with $10 \mu\text{L}$ of pure water. The black lines in (A) and (B) correspond to the supernatant from the 1st washing step, and the red and blue lines correspond to the supernatants obtained after the 2nd and the 3rd washing step, respectively. (C) Photographs of 0.6-mL microcentrifuge tubes containing $\text{SiO}_2/9\text{-AA}$ nanoparticles – after washing with $\text{NH}_3(\text{aq})/\text{water}$, and centrifugation (10000 rpm, 10 min). Note that the pellets became pale after the treatment with $\text{NH}_3(\text{aq})$ (C), which indicates the 9-AA had been leached from the $\text{SiO}_2/9\text{-AA}$ nanoparticles.

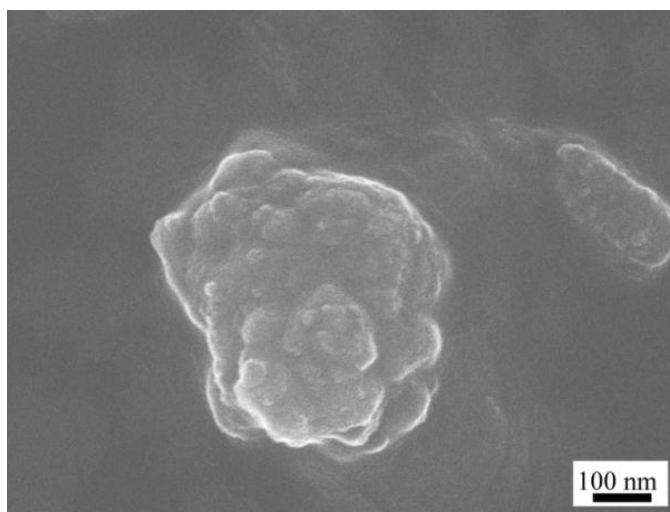


Figure 2.8 Scanning electron micrographs of SiO₂/9-AA nanoparticles following incubation in NH₃(aq) solution for 30 min.

This species has rod-shaped cells ($\sim 350 \times 40 \mu\text{m}$). Since cell wall in algal cells is rich in anion-forming biomolecules (*e.g.* galacturonic acid – a component of pectin),⁵⁸ the SiO₂/9-AA nanoparticles can readily attach onto the outer surface of the cell due to electrostatic interactions (**Figure 2.9**). **Figure 2.10** presents optical and fluorescence micrographs of individual *C. acerosum* cells with/without SiO₂/9-AA nanoparticles. Red fluorescence originates from the natural dyes present in the cell, while yellow fluorescence originates from SiO₂/9-AA nanoparticles attached onto the cell surface. We also tested the new matrix with another species of algae – *Anabaena* sp.: also in this case, the SiO₂/9-AA nanoparticles readily attached to the outer surface of the cells (**Figure 2.11**). We noted that, following the incubation with the SiO₂/9-AA nanoparticles, heterocysts of *Anabaena* sp. – which normally do not fluoresce at the $\lambda_{\text{ex}} = 330\text{-}380 \text{ nm}$ – started to fluoresce with blue light. One can speculate the cell wall in heterocysts contains more anionic components which can bind a greater amount of the SiO₂/9-AA nanoparticles, as compared with the photosynthesizing cells.

Following the treatment of *C. acerosum* cells with SiO₂/9-AA nanoparticles (**Figures 2.10** and **2.12A**), and subsequent exposure of the sample to ammonia vapors, we used

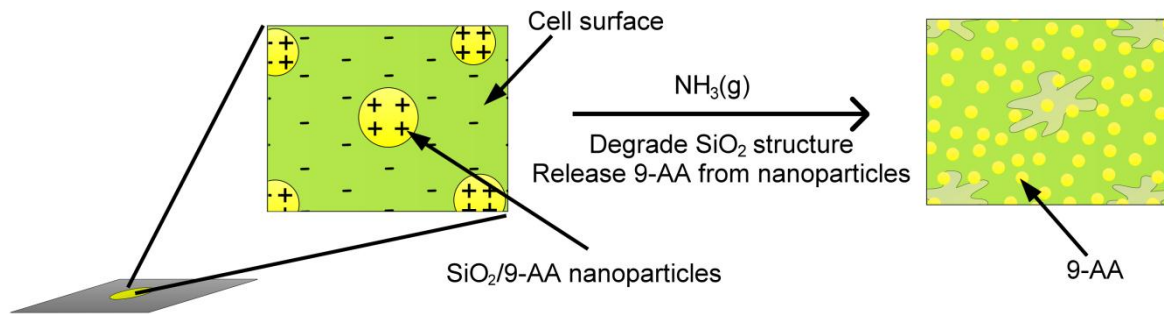


Figure 2.9 Putative mechanism of the adsorption of SiO₂/9-AA nanoparticles on algal cells followed by the controlled release of 9-AA.

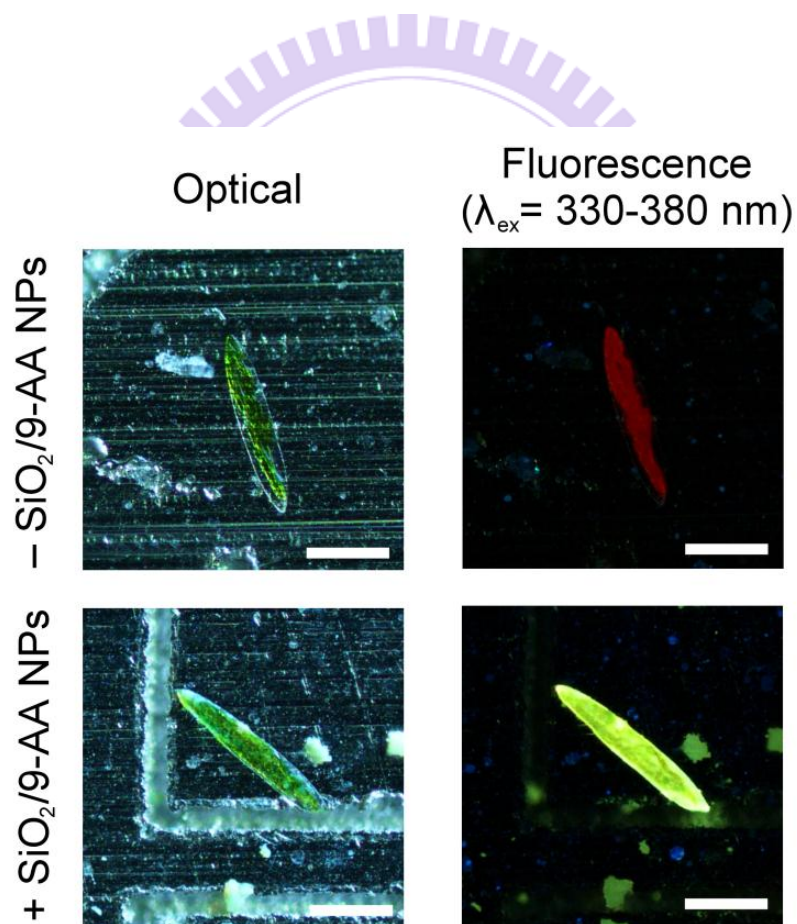


Figure 2.10 Optical and fluorescence micrographs of individual *Closterium acerosum* cells with/without SiO₂/9-AA nanoparticles. Scale bars: 200 μm .

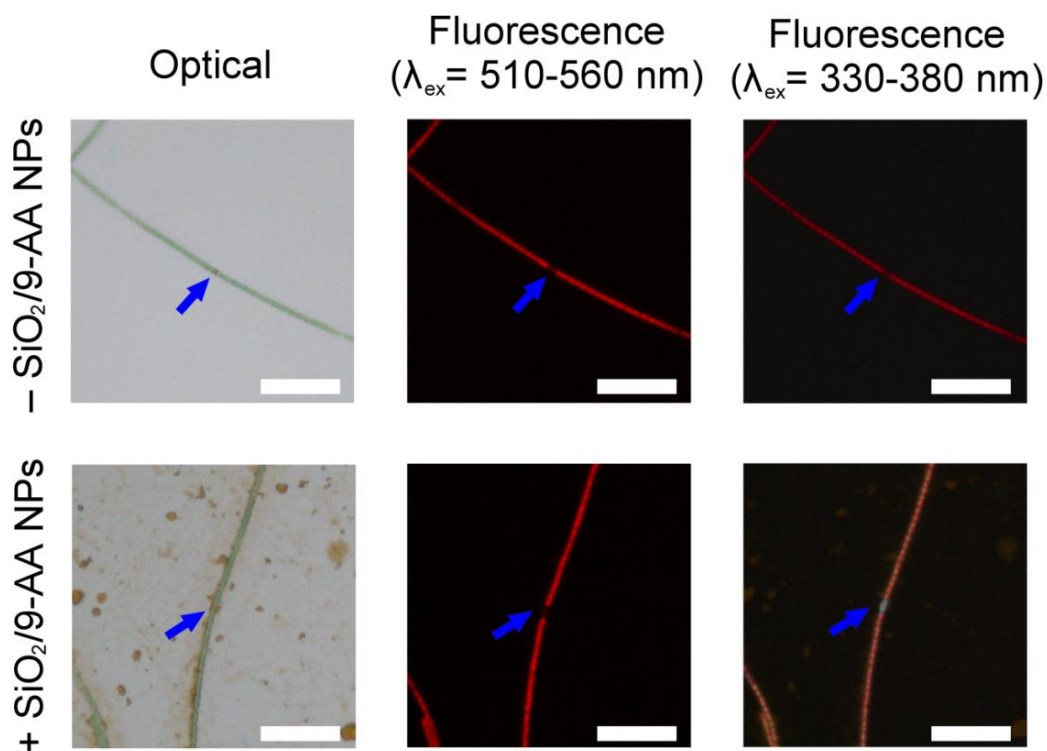


Figure 2.11 Optical and fluorescence micrographs of *Anabaena* sp. with/without SiO₂/9-AA nanoparticles (0.5 μL, 5 mg mL⁻¹). The fluorescence micrographs were obtained using two different excitation wavelengths ($\lambda_{\text{ex}} = 510\text{-}560$ and $330\text{-}380$ nm – middle and right, respectively). Blue arrows indicate heterocysts. Scale bars: 50 μm.

MALDI-MS to obtain spectra of single cells. **Figure 2.12B** shows a mass spectrum of *C. acerosum* with three high signals at the m/z 709.4, 779.5, and 815.5. We further conducted MS/MS analysis of these three ions by analyzing their post-source decay products using the laser-induced fragmentation technology (LIFT) cell. The presence of three fragments – PO₃⁻ (m/z 97), H₂PO₄⁻ (m/z 97), and C₃H₆O₅P⁻ (m/z 153) – suggests that the three signals are related to analytes from the group of phospholipids (**Figure 2.14**). We confirmed the identities of these peaks by performing MALDI-MS analysis with internal calibrants (**Table 2.1**). Matching the measured and the predicted m/z values led to a tentative identification of the three metabolites as phosphatidylglycerols.

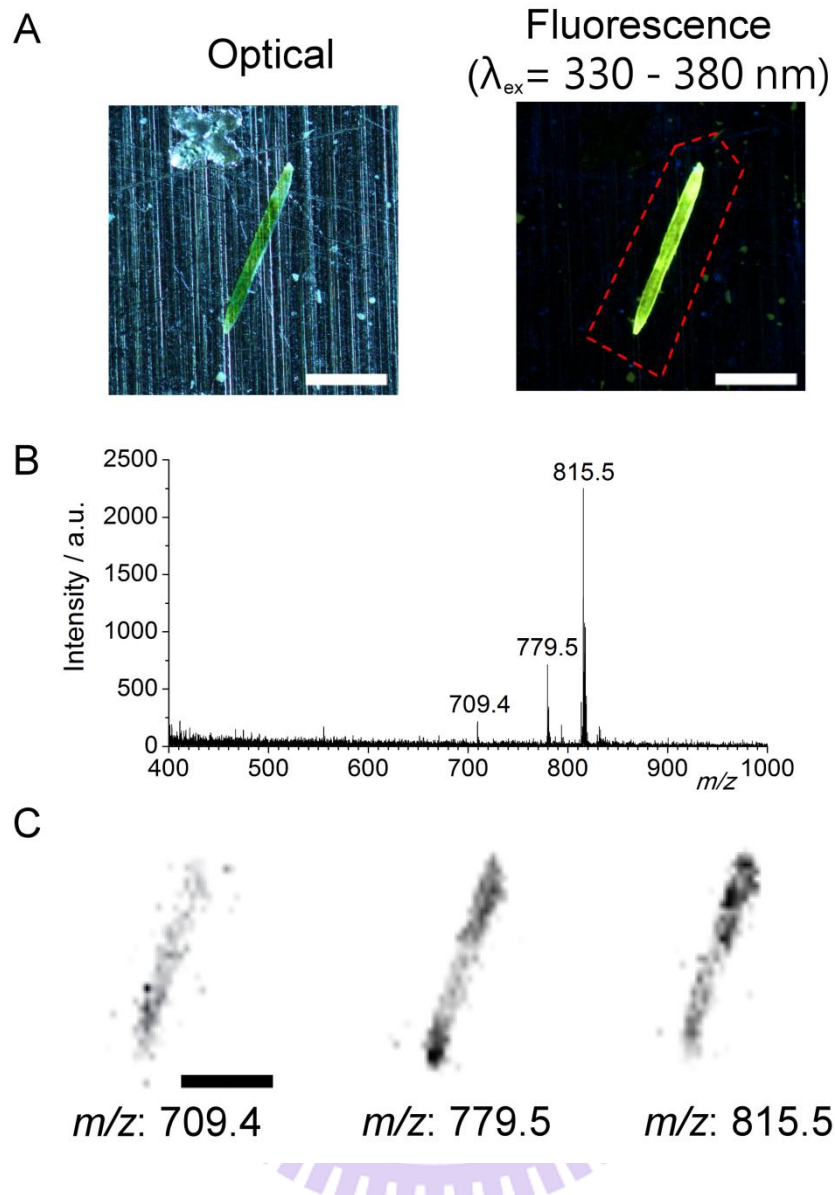


Figure 2.12 Single-cell MS imaging with SiO₂/9-AA nanoparticles used as matrix. (A) Optical and fluorescence micrographs of a single *Closterium acerosum* cell with the attached SiO₂/9-AA nanoparticles. (B) MALDI mass spectrum of a single cell of *Closterium acerosum* – following the occlusion with SiO₂/9-AA nanoparticles, and the release of 9-AA induced by gaseous ammonia. The blank spectrum of SiO₂/9-AA nanoparticles shows no peaks overlapping with the three sample-related peaks (**Figure 2.13**). (C) Mass spectrometric images of a single cell of *Closterium acerosum* (same as in (A)). The MS images were obtained in the negative-ion mode by MALDI-time-of-flight (TOF)-MS. Laser beam wavelength: 355 nm; frequency: 50 Hz; diameter: 10 μm; raster spacing: 15 μm. The red-color dashed line in (A) approximately delimits the MS imaging area in (C). Scale bars: 200 μm.

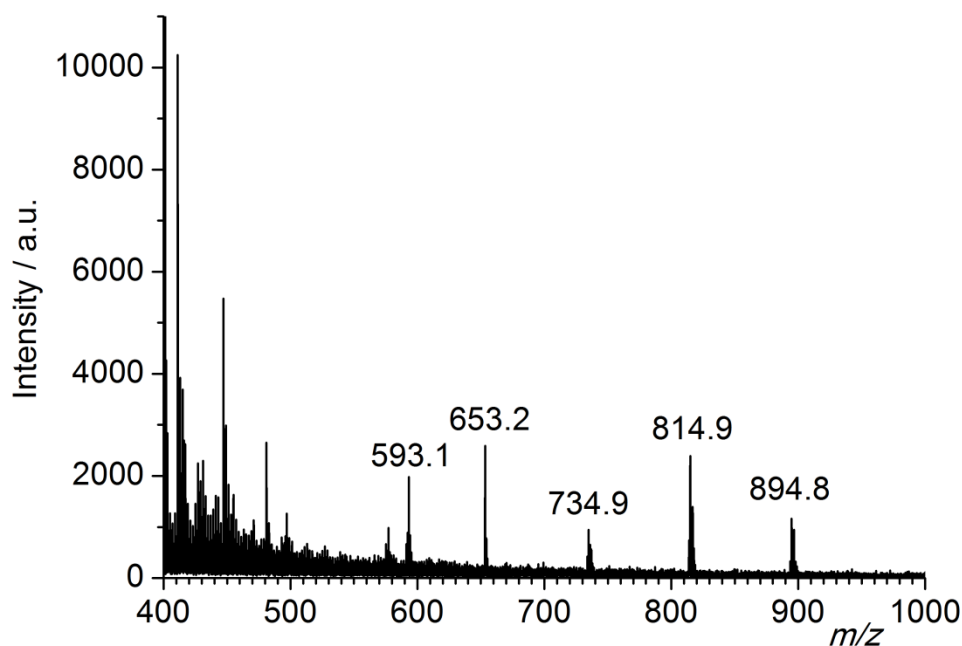


Figure 2.13. MALDI mass spectrum of SiO₂/9-AA nanoparticles deposited on an aluminum plate, and incubated with gaseous ammonia (blank). Note that the signal at the m/z : 814.9 – in this blank spectrum – does not completely overlap with the signal at the m/z : 815.5 – recorded when analyzing the sample of *Closterium acerosum* cells (cf. **Figure 2.12**).

The three prominent MS signals (m/z 709.5, 779.5, and 815.5) were subsequently monitored in a MALDI imaging sequence (**Figure 2.12**) using a 10- μ m UV laser beam, and a raster with 15- μ m spacing. The MS signals follow the contours of single cells as observed in the optical and fluorescence images (**Figure 2.12A**). Although the coverage of the cell with MALDI matrix is highly homogeneous (**Figures 2.12A, 2.10** and **2.14**), the distribution of metabolites within the cell – as visualized by MALDI-MS – is seen to represent some heterogeneity (**Figure 2.12C**): this points out the advantage of performing MALDI-MS imaging with subcellular resolution. For example, the metabolite corresponding to the MS signal at the m/z 779.5 seems to be present in the whole cell, while the metabolites corresponding to the MS signals at the m/z 709.5 and 815.5 appear to be more concentrated in one of the two semicells of the *C. acerosum* cell under investigation (**Figure 2.12C**).

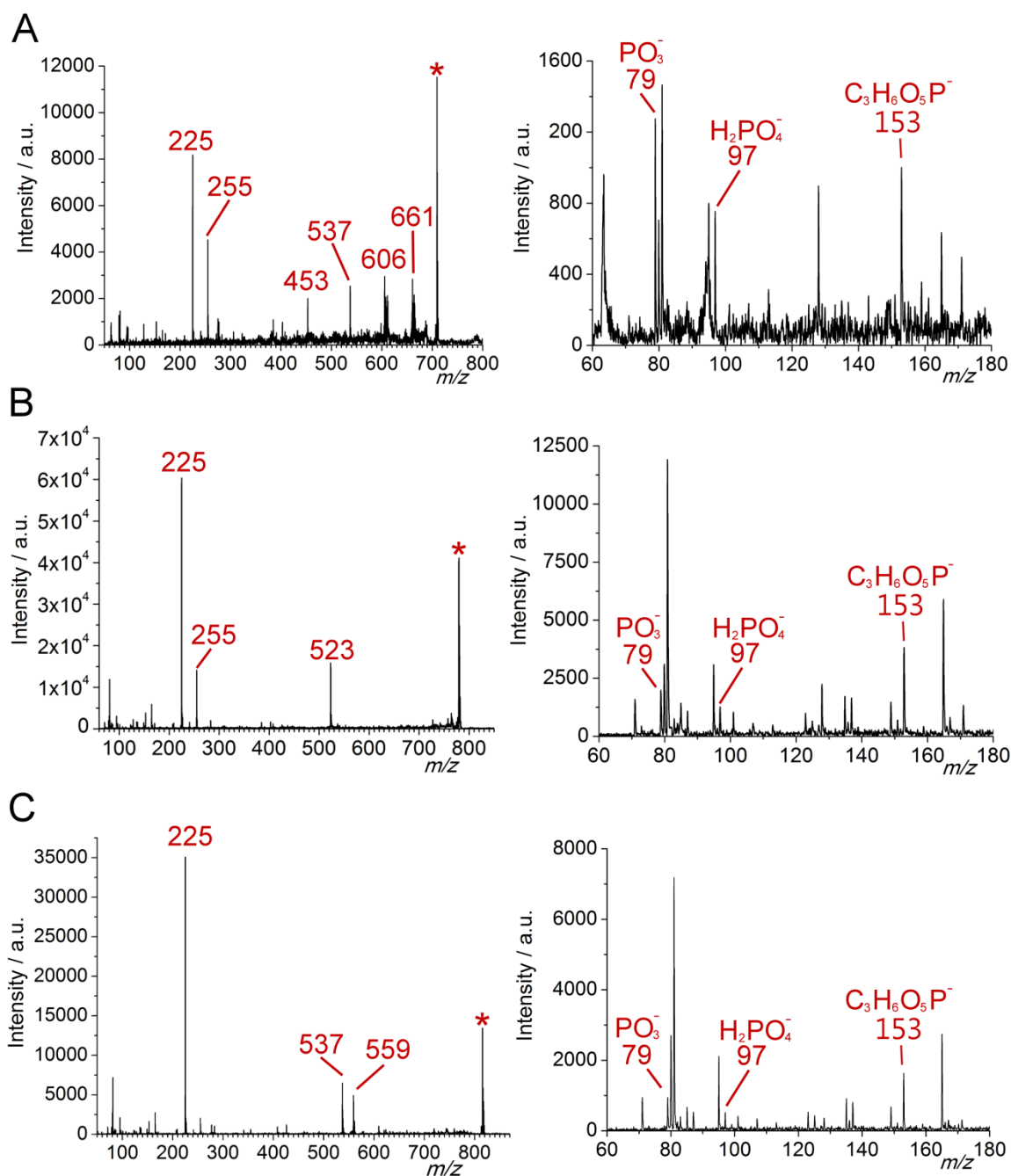


Figure 2.14 MALDI-MS/MS spectra of the three ions corresponding to the MALDI images depicted in **Figures**

2.12 and **2.15**: (A) m/z 709.4, (B) m/z 779.5, (C) m/z 815.5. Precursor ions are marked with asterisks (*).

The traces in the left-side column represent full m/z -range spectra whereas the traces in the right-side column display the low- m/z range (within the same spectra). The tandem mass spectra were obtained from the samples of *Closterium acerosum* (co-crystallized with 9-AA) in the negative-ion mode, using the laser-induced fragmentation technology (LIFT).

Table 2.1 Matching the observed and the predicted m/z values after the analysis of *Closterium acerosum* cells by negative-ion MALDI-TOF-MS using 9-aminoacridine as matrix, and in the presence of internal calibrants. The internal calibrant mixture contained adenosine triphosphate, guanosine triphosphate, uridine diphosphate glucose, acetyl coenzyme A and bradykinin acetate (each at the concentration of 8.33×10^{-6} M).

Observed m/z	Predicted formula	Predicted m/z [M-H] ⁻	$ \Delta m $ (Da)
709.379	C ₃₈ H ₆₃ O ₁₀ P	709.40861	0.03
779.510	C ₄₃ H ₇₃ O ₁₀ P	779.48686	0.02
815.500	C ₄₆ H ₇₃ O ₁₀ P	815.48484	0.02

High-quality images of single *C. acerosum* cells were obtained using either 15 and 10- μm laser scan rasters (**Figures 2.12C** and **2.15**, respectively). In the case of *Anabaena* sp., the method allowed imaging individual chains of cells (thickness < 10 μm ; **Figure 2.16**). Further improvement in lateral resolution is expected after combining the sample preparation using the SiO₂/9-AA nanoparticle matrix (proposed here) with state-of-the-art MALDI-MS instruments which use laser beams with diameters smaller than 10 μm .

Coating specimens with chemical matrices is seen to be a big challenge in MALDI imaging. Common coating methods involve pneumatic spray and electrospray deposition [for reviews, see refs 16, 17, 21]. Since matrix compounds are normally dissolved in organic solvents, spray-based methods cause analyte to spread over the sample surface.^{17,21} Several alternative ways of applying matrix prior to MALDI-MS imaging have been proposed to date: for example, matrix can be deposited on the sample by using inkjet printing, which produces an array of matrix spots, the method which is mainly applicable for imaging at low lateral resolution.⁵⁹ The matrix sublimation/recrystallization method ensures small crystal size, high

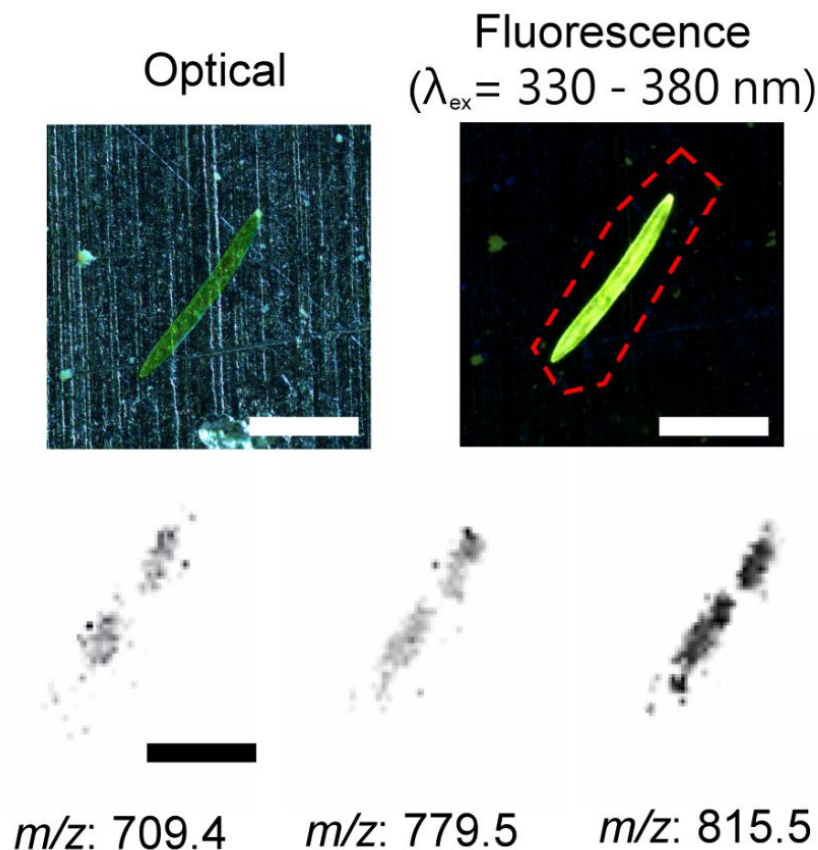


Figure 2.15 Optical and fluorescence micrographs (top) as well as mass spectrometric images of a single cell of *Closterium acerosum* (bottom). The fluorescence micrograph ($\lambda_{\text{ex}} = 330\text{-}380 \text{ nm}$) shows the presence of $\text{SiO}_2/9\text{-AA}$ nanoparticles (yellow color) on the cell surface (before the exposure to gaseous ammonia). MS images were obtained in the negative-ion mode by MALDI-TOF-MS. Laser beam wavelength: 355 nm; frequency: 50 Hz; diameter: 10 μm ; raster spacing: 10 μm . Scale bars: 200 μm .

homogeneity, and minimum dispersion of analytes; however, this method is not suitable for all kinds of samples and matrices.^{22,23,25} Here we showed that high lateral resolution can be achieved after replacing conventional matrix application protocols with hybrid nanoparticles used as matrix carriers. Since the nanoparticles are dissolved in water – and the organic matrix release occurs *in situ*, when triggered by ammonia vapors – this way of preparing samples for MS does not blur the native distributions of the analytes, and the so-called “sweet spot” effect may be reduced.

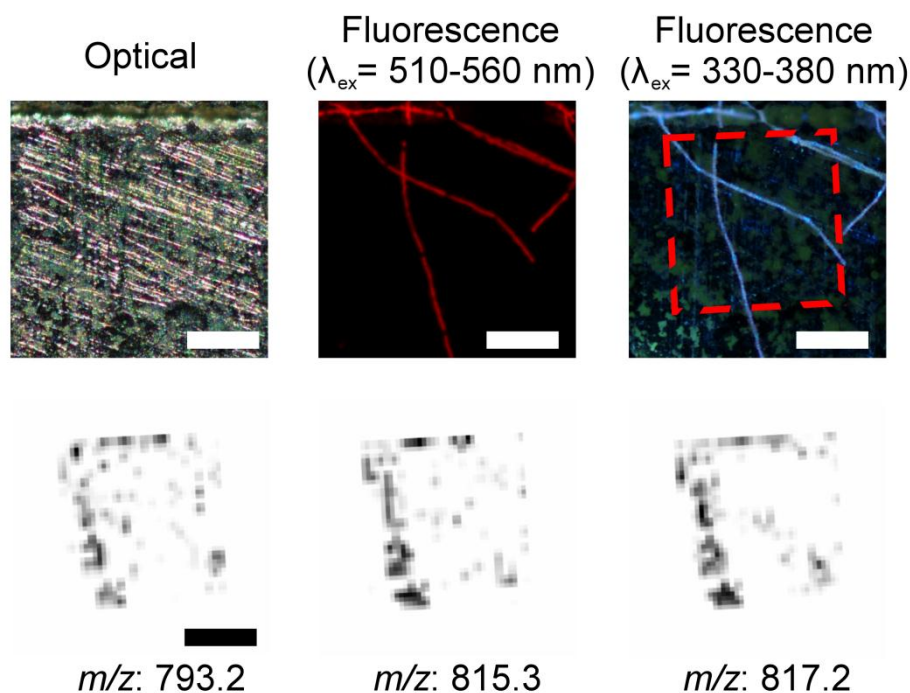
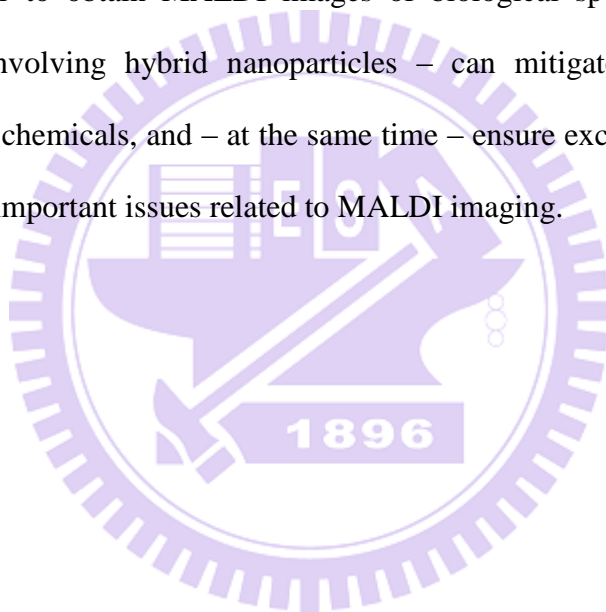


Figure 2.16 MALDI-MS imaging of small cell ensembles using *Anabaena* sp. as a model. Optical and fluorescence micrographs (top) obtained using two different excitation wavelengths ($\lambda_{\text{ex}} = 510\text{-}560$ and $330\text{-}380$ nm – middle and right, respectively) and MALDI-MS images of *Anabaena* sp. (bottom) after the treatment with $\text{SiO}_2/9\text{-AA}$ nanoparticles and ammonia vapors. The MS images were obtained in the negative-ion mode by MALDI-TOF-MS. Laser beam wavelength: 355 nm; frequency: 50 Hz; diameter: 10 μm ; raster spacing: 10 μm . The red-color dashed line in approximately delimits the MS imaging area. Scale bars: 100 μm .

2.4. Concluding remarks

To our knowledge, this is the first study demonstrating a hybrid inorganic-organic nanomaterial designed with the purpose of mapping metabolites in microscale biological specimens by mass spectrometry. This novel strategy brings about several key advantages: (i) application of the hybrid matrix can be conducted in liquid phase (native environment of the biological cells), (ii) the matrix targets the biological specimen by attaching to its surface due to electrostatic interactions, (iii) application of the organic MALDI matrix compound occurs

in situ, following the attachment of nanoparticles, and the controlled-release step (in alkaline vapors), which warrants less dispersion of analytes than using standard matrix application techniques, (iv) the expenditure of chemicals is minimized. Another aspect of this analytical strategy is related to labwork safety: The implementation of many standard chemistry and biochemistry procedures may be hazardous to researchers and pose threat to the environment, for example: carcinogenic ethidium bromide is frequently used as a DNA marker in gel electrophoresis, solvents such as tetrahydrofuran or chloroform are used in synthetic protocols despite their explosive nature, eventually – toxic matrices are sprayed using gas-powered painting guns in order to obtain MALDI images of biological specimens. The proposed imaging strategy – involving hybrid nanoparticles – can mitigate the exposure of the experimenters to toxic chemicals, and – at the same time – ensure excellent lateral resolution; therefore, it addresses important issues related to MALDI imaging.



Chapter 3

Recording temporal characteristics of convection currents by continuous and segmented-flow sampling

3.1. Introduction

A vast majority of contemporary developments and applications in liquid-phase chemistry deals with homogeneous solutions. Organic chemists pay a lot of attention to adequate mixing of the reaction mixtures; inhomogeneities could result in a decreased reaction efficiency, or produce system instabilities. In analytical chemistry, homogenisation of samples is essential for ascertaining reliable and reproducible results. However, many natural and human-triggered processes are non-homogeneous; examples include the diffusion of atmospheric gases into ocean waters, and dispersion of environmental pollutants in the atmosphere, or in water reservoirs. Chemical gradients are omni-present in the macro-world and micro-worlds: for example, organisms emit signalling molecules into their habitats while individual cells do the same in their microenvironments in order to exert a response of other biological entities. Diffusion and convective mixing further contribute to the dispersion of these chemical species until an equilibrium is reached. On the sub-cellular and supra-cellular levels, chemical gradients are responsible for the evolution of important physiological processes.

Analytical methods for studying the propagation of chemical waves in non-equilibrated mixtures are scarce. For instance, when analyzing three-dimensional samples using

spectrophotometric tools, one has to assume a perfect homogeneity of a solution, so that the absorption laws are obeyed (*cf.* section 1.4). Therefore, spectrophotometry in its standard format is not directly applicable to the analysis of chemical heterogeneity. Same holds for the modern analytical techniques such as mass spectrometry (MS), in which case samples are typically loaded into syringes in order to infuse them via electrospray ionization (ESI) emitter into MS orifice; this normally eliminates the possibility of studying chemical gradients present in liquid media.

As outlined in section 1.5, Traditional sampling methods employing capillary tubing or microfluidic devices are likely to blur the spatiotemporal gradients due to advection and diffusion. Although Taylor dispersion of sample plugs transported in microfluidic channels can be reduced by implementing electrokinetic flow, electric fields are not always compatible with the samples studied. Sampling by segmented flow may readily be achieved by simultaneous injection of two immiscible fluids into a capillary or a microfluidic channel.^{27,28} A considerable advantage of segmented flow is that one can reduce the dispersion of analytes as the discrete samples are transported along the flow line. In analytical protocols, segmented flow systems can readily be coupled with various types of analytical instruments; in fact, this approach has widely been used in enzyme assays,^{60,61} protein analysis,^{62,63} small molecule analysis,^{32-34,64} and single-cell analysis.^{65,66} Segmented flow can also be used in conjunction with various detection platforms, including nuclear magnetic resonance⁶⁷ and mass spectrometry (MS).⁶⁸⁻⁷¹

Building on the previous work, here we show two facile methods for recording spatiotemporal gradients formed during convection of substances in liquid media – used as a model process showing the dynamics of chemical heterogeneity in the three-dimensional space. The methods presented here are either based on continuous or segmented flow fluid transport, and used in conjunction with visible-range absorbance and/or mass spectrometric detection.

3.2. Materials and methods

3.2.1. Materials

Acetic acid, caffeine, ferroun, and *n*-octanol were purchased from Sigma-Aldrich (St Louis, USA). Blue ink (Simbalion, New Taipei City, Taiwan) was purchased from a local stationery shop. The fused silica capillary with the ID 150 μm (OD 375 μm) was purchased from GL Science (Tokyo, Japan), while the fused silica capillary with the ID 320 μm (OD 435 μm) and ID 450 μm (OD 673 μm) were purchased from Polymicro (Phoenix, USA). Tygon tubing was purchased from Saint Gobain (Akron, USA) and IDEX (Oak Harbor, USA).

3.2.2. Construction of the flow-through optical detector

The multi-point tri-wavelength flow-through optical detector enables measuring the absorbance of sample plugs delivered in segmented or continuous flow (**Figure 3.1A** and **3.1B**). It comprises 8 photoresistors (diameter: ~ 5 mm; CdS type; resistance range: 8-20 k Ω ; purchased from a local electronics shop) and 8 tri-colour light emitting diodes (LEDs; diameter: ~ 5 mm; 4 pins, common anode; diffuse light; power angle 20-25 $^\circ$; measured wavelengths: $\lambda_{\text{red}} = 629 \pm 6.5$ nm, $\lambda_{\text{green}} = 518 \pm 16$ nm, $\lambda_{\text{blue}} = 463 \pm 11$ nm; purchased on eBay). The silica capillary acts as a flow line as well as an optical cell with 8 detection windows. The wavelength of the emitted light can be changed sequentially, or alternatively, the LEDs in the neighbouring detection channels can be set to emit light in different wavelengths.

The optical cell was incorporated into a plastic casing with 8 holes with a diameter of 4.1 mm, spaced at 8 mm (**Figure 3.1A**, left panel). The inner surface of the casing was lined with aluminium foil. An infrared μs -laser engraving machine (Huahia Laser, Taipei, Taiwan) was used to create eight pinholes (diameter, ~ 450 μm) in the aluminium foil. The pinholes were spaced in a way that they exactly overlapped with the centre of the capillary used as the optical cell. Polyimide coating was removed from a standard GC-type fused silica capillary

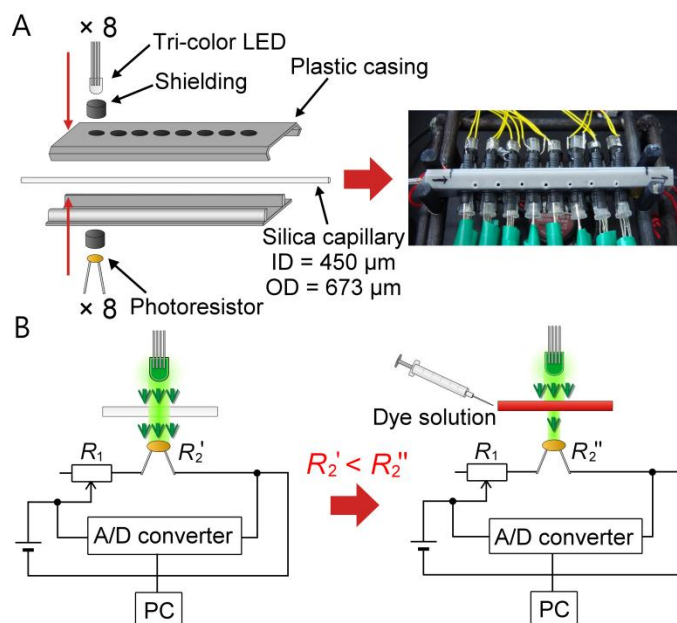


Figure 3.1 Multi-point multi-wavelength flow-through optical detector. (A) Assembly of the device. (B) Absorbance measurement in an individual channel. Note that only up to 3 channels were used in this study.

(length: 12 cm; ID 450 μm, OD 673 μm) – used as the optical cell – and the transparent section of the capillary was precisely aligned with the pinholes along the aluminium foil lining inside the plastic casing. The two parts of the plastic casing were joined together, so that the positions of the LEDs on one side matched the positions of the photoresistors mounted on the opposite side (**Figure 3.1A**, left panel). Smaller holes (diameter ~ 1 mm) were drilled in the plastic casing in order to increase air circulation (**Figure 3.1A**, right panel). The optical cell assembly was installed inside a styrofoam box (inner dimensions: 24 × 22 × 10 cm, w/d/h). Three PC-type electric fans were also installed in the box to enhance air circulation, and to facilitate heat dissipation. The fused silica capillary was connected to the upstream and the downstream parts of the flow line with Tygon tubing (ID 0.38 mm, OD 2.2 mm).

The wavelength of the light emitted by the tri-colour LEDs was controlled by the relay

board (Denkovi Assembly Electronics, Byala, Bulgaria). An analog/digital data logger (ADC-20; resolution: 20 bits; input range: ± 2.5 V; preset sampling rate: 61-183 ms data-point⁻¹; Pico Technology, St Neots, United Kingdom) was used to record the electric potentials at the outputs of the photoresistor circuits. Both devices were connected to a computer via USB ports, and operated with appropriate software packages. The segmented-flow data were treated using a custom software written in Free PASCAL (version 1.0.10 2009/04/10; B. Gábor, P. Muller, P. Vreman); the algorithm automatically removed the features due to *n*-octanol segments, and preserved the features due to the water-based segments.

3.2.3. Assembly of the three-port Y-junction for generating segmented flow

The design of the segmented flow generator is shown in **Figure 3.2**: Two fused silica capillaries (length: 2.5 cm; ID 320 μm ; OD 435 μm), connected with Tygon tubing (ID 0.25 mm, OD 2.07 mm), were inserted to another piece of Tygon tubing with an ID of 0.7 mm (OD 3.2 mm). The distance between the outlets of the two fused silica capillaries (inside the 0.7-mm ID section of Tygon tubing) was ~ 5 mm. The resulting junction was then sealed with Epoxy glue (plastic steel Epoxy resin; PowerBon, New Taipei City, Taiwan), and after setting for ~ 1 h, the whole assembly was ready for use. In order to produce segmented flow, water and *n*-octanol (immiscible phases) were delivered via the inlet ports (**Figure 3.2**).

3.2.4. Measurements using the system coupled with a mass spectrometer

Hyphenating different detection systems in order to attain orthogonal chemical information is an important area of analytical science. In this study, we also coupled the home-made multi-point multi-wavelength detector with a mass spectrometer, so as to enable simultaneous monitoring of spatiotemporal gradients by two detection systems. Careful optimization of the experimental setup was necessary in order to select the flow rates which are suitable for the studied process (convection), and optical as well as mass spectrometric

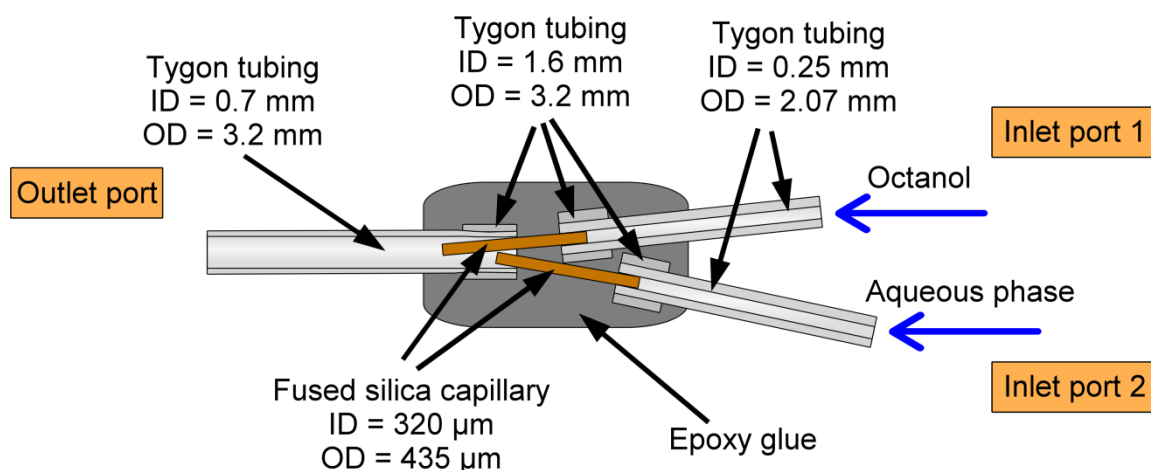


Figure 3.2 The design of the Y-junction used to generate segmented flow.

detection. Pumping too much sample towards the orifice of the mass spectrometer may invite contamination of the instrument. On the other hand, decreasing flow rate during the sampling will also decrease the temporal resolution of the method. By implementing the “split-flow” approach, and adjusting backpressures in the flow line, it was possible to achieve workable conditions for this setup.

When using such a hyphenated system, several modifications had to be introduced to the convection chamber and the sampling probe: Two fused silica capillaries (length: 6 cm; ID 320 μm ; OD 435 μm) were transferred through the septum in the cap (18-MSL-ST3; Thermo Fisher Scientific, Waltham, USA) of the 20-mL glass vial (20-HSV; Thermo Fisher Scientific) acting as the “convection” chamber. One of these capillaries was connected to the syringe pump, and the other one was connected to the downstream flow line (Tygon tubing) with the optical detector and the mass spectrometer. The fused-silica capillary used as the ESI emitter (length: 2 cm; ID 150 μm ; OD 375 μm) was mounted in a tiny hole made in the Tygon tubing (ID 0.38 mm). The distance between the ESI emitter and the orifice of the ion trap MS was relatively long (~ 2 cm) in order to prevent contamination of the instrument when

concentrated samples were analyzed. Since the section of Tygon tubing mounted downstream from the ESI emitter exerted slight backpressure on the liquid in the flow line, a small portion of the liquid was diverted to the fused silica capillary section acting as the ESI emitter. Recently, a method of introducing samples to mass spectrometers without the need for establishing an electrical connection at the emitter was published.⁷² In our system, we also skipped the electrical connection at the ESI emitter, which simplified the design and operation of the system without damaging its performance. In this study, we used the amaZon speed ion trap mass spectrometer from Bruker Daltonics (Bremen, Germany). The voltage applied to the ion transfer capillary was -5500 V (positive-ion mode), and the end-plate offset was set to 500 V. The flow rate of the dry gas was set to 12 L min⁻¹. The mass range was 70-380 Da, and the accumulation time was 0.5 ms.

At the beginning of the experiment, before acquiring data, the test analyte (ferroin) was injected into the lower part of the glass vial filled with ~ 21 mL of an aqueous solution containing caffeine (4.8×10^{-5} M) and acetic acid (0.5 %). The data acquisition started when the syringe pump was turned on, and 0.5%-solution of acetic acid was pumped into the vial. Since the vial was completely filled with the liquid medium, the acetic acid solution – injected with the syringe pump – exerted hydrodynamic pressure on its contents; as a result, the liquid medium was pushed out via the second capillary mounted in the septum. This setup provided an adequate flow stability for the continuous MS analysis.

3.2.5. Measurement of the flow rate in the ESI emitter

In order to measure the effective flow rate of the sample in the ESI emitter, we implemented the experimental setup shown in **Figure 3.3**. Water was pumped along the flow line by syringe pump at the flow rate of 30 μ L min⁻¹. Effluent was collected at the outlet of the Tygon tubing (length: 30 cm; ID 0.13 mm) during 10 min. The net weight of the effluent aliquots was determined using analytical balance. The procedure was performed with the

mass spectrometer on and off, and also after the removal of the ESI emitter. The flow rate of liquid sample in the ESI emitter was then calculated by subtraction of the flow rates determined for the eluate collected at the outlet of the Tygon tubing (**Figure 3.3A**) – without and with ESI emitter installed (**Figure 3.3B**).

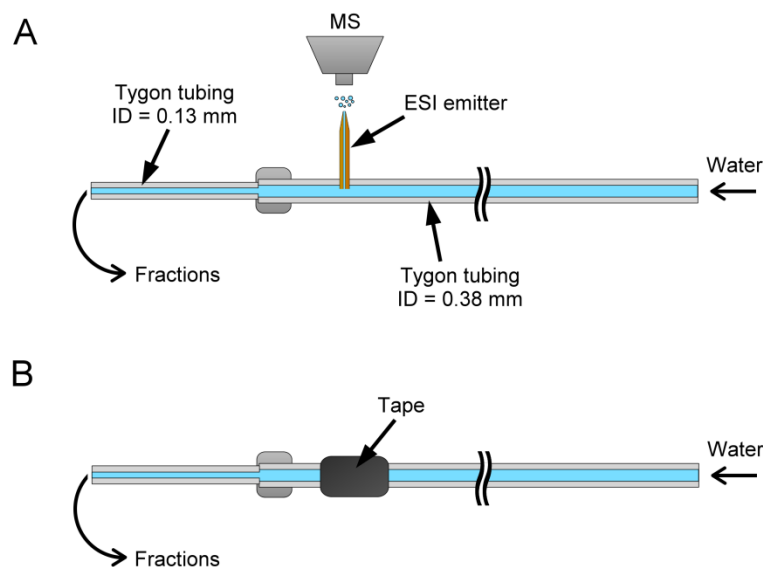


Figure 3.3 Measurement of the effective flow rate in the fused silica capillary used as ESI emitter. (A) The ESI emitter is installed in the flow line, and the MS is on. (B) The ESI emitter is taken away, and adhesive tape is used to prevent leakage of the liquid medium through the small hole made in the wall of the Tygon tubing.

3.3. Results and discussion

3.3.1. Monitoring convection-driven currents by optical detector

absorbance detection

Here we demonstrate probing chemical waves, which are formed in a liquid medium due to convection, by using continuous flow sampling in conjunction with optical absorption detection. A small amount of medium is sampled and transferred along the capillary flow line

towards detector by using either segmented flow or non-segmented (continuous) flow. At the beginning of the experiment, we injected a small aliquot of ferroin solution into the bottom of a 20-mL glass vial. Subsequently, the lower part of the vial was heated up ($\sim 34\text{ }^{\circ}\text{C}$) in order to develop a temperature gradient, and induce convective mixing of the ferroin solution with the liquid medium present in the vial. We used a syringe pump operated in the withdrawal mode in order to pull the contents of the vial with the flow rate of $30\text{ }\mu\text{L min}^{-1}$. *n*-Octanol was simultaneously injected to the Y-junction (installed along the flow line) by a syringe pump operated in the infusion mode at the flow rate of $6\text{ }\mu\text{L min}^{-1}$ (**Figure 3.4**). The volume of each aqueous plug is estimated to 1.25 ± 0.16 (SD) μL .

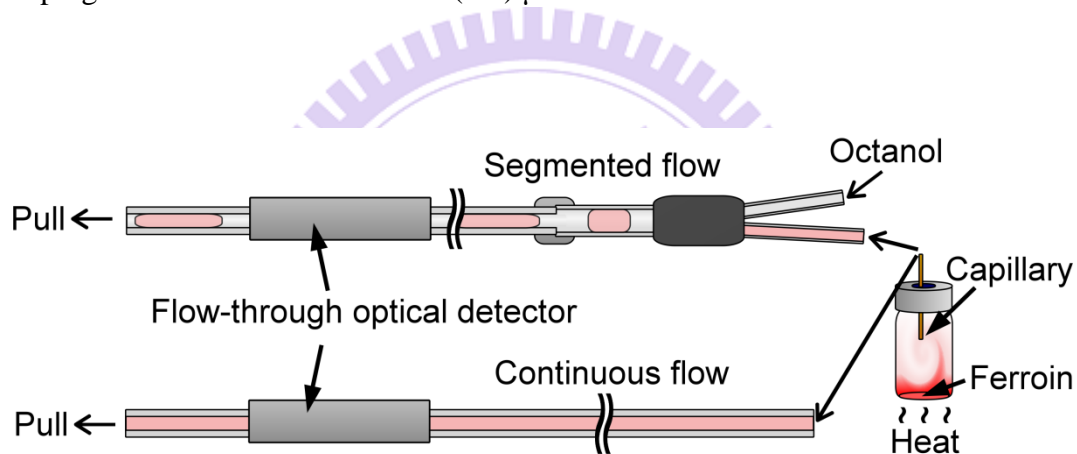


Figure 3.4 Recording convection with segmented and continuous flow. (A) Experimental setup used in the real-time sampling with/without segmented flow prior to detection by the flow-through optical detector (*cf.* **Figure 3.1**). The segmented flow was generated by pushing *n*-octanol towards the Y-junction while the bulk of the liquid was withdrawn by a syringe pump at the outlet of the flow line.

Figure 3.5 shows photographs of the inlet vial representing the convection-driven mixing of ferroin (red) with the liquid medium (transparent) while **Figure 3.6** shows the corresponding raw data. The “ups” and “downs” in the original signal trace are caused by the differences in refractive indices and extinction coefficients of *n*-octanol and the aqueous samples. The relative heights of the lower section of the valleys in **Figure 3.6** vary according

to the absorbance of the plugs sampled from the vial. In order to simplify the representation of the data, a custom software was used to remove the signal of *n*-octanol, and the data treated this way are displayed in **Figure 3.7A** (red line). From this data it is clear that the signal increased due to the increasing absorbance of ferroin. Interestingly, the increase of the absorbance with time (in relative units) cannot be described by any simple function, as one could do for the diffusion process. The gradual mixing of ferroin with the liquid medium is a chaotic process, and the trace in **Figure 3.7A** (red line) represents numerous fluctuations before the signal stabilizes at a level when the mixture became a homogeneous solution.

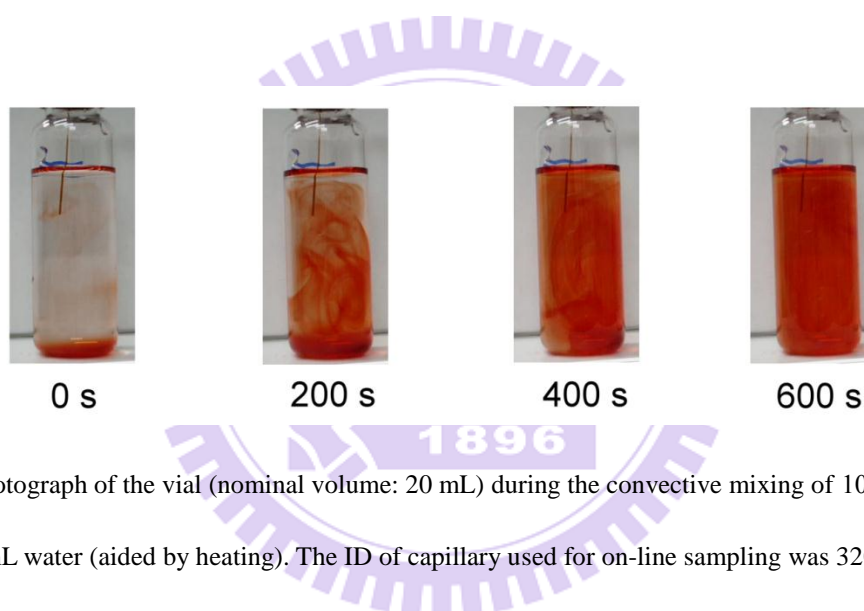


Figure 3.5 Photograph of the vial (nominal volume: 20 mL) during the convective mixing of 100 μ L ferroin with 15 mL water (aided by heating). The ID of capillary used for on-line sampling was 320 μ m.

Next, we carried out a similar experiment but using this time continuous (non-segmented) flow to transfer samples from the glass vial to the detector. This yielded curves which also represent some fluctuations (**Figure 3.7B**, red line). However, in this case, the traces are much smoother than the curves obtained using segmented flow (**Figure 3.7A**, red line). This unwanted “smoothing effect” is due to advection and diffusion (*e.g.* ref. 73), taking place in the flow line – between the sample inlet and the detector. Compared with the continuous flow (**Figure 3.7B**), the segmented flow (**Figure 3.7A**) helps to preserve temporal

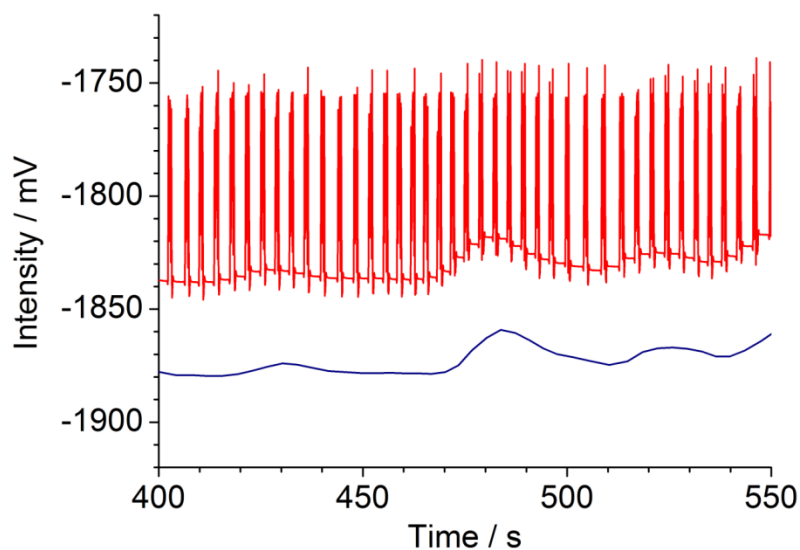


Figure 3.6 Convective mixing of ferroin with water followed by segmented flow and flow-through optical detector (*cf.* **Figure 3.1**; wavelength: 518 nm). The red line represents original data while the blue line shows the final data extracted by the custom software. The two traces were shifted vertically for clarity.

and spatial resolution of the digitized three-dimensional sample (*cf.* **Figure 3.5**).

In both cases, the traces can be fit with exponential functions (**Figure 3.7A** and **3.7B**, blue dashed line), which represent the mixing trends. Apart from the fluctuations caused by convection currents, the equilibriums are reached at similar times (taking into account the small difference between the effective sampling flow rates in the segmented-flow and continuous flow systems). In **Figure 3.8**, the experimental data (*cf.* **Figure 3.7A** and **3.7B**, top graphs, red line) were subtracted with the values predicted by the fitted exponential functions (*cf.* **Figure 3.7A** and **3.7B** top graphs, blue dashed line): this representation highlights the presence of strong fluctuations of relative absorbance due to the convection process. These fluctuations are especially apparent in the middle of the data record, *i.e.* 400-800 s (segmented flow, **Figure 3.8A**), and 300-700 s (continuous flow, **Figure 3.8B**). From **Figure 3.7A** it is

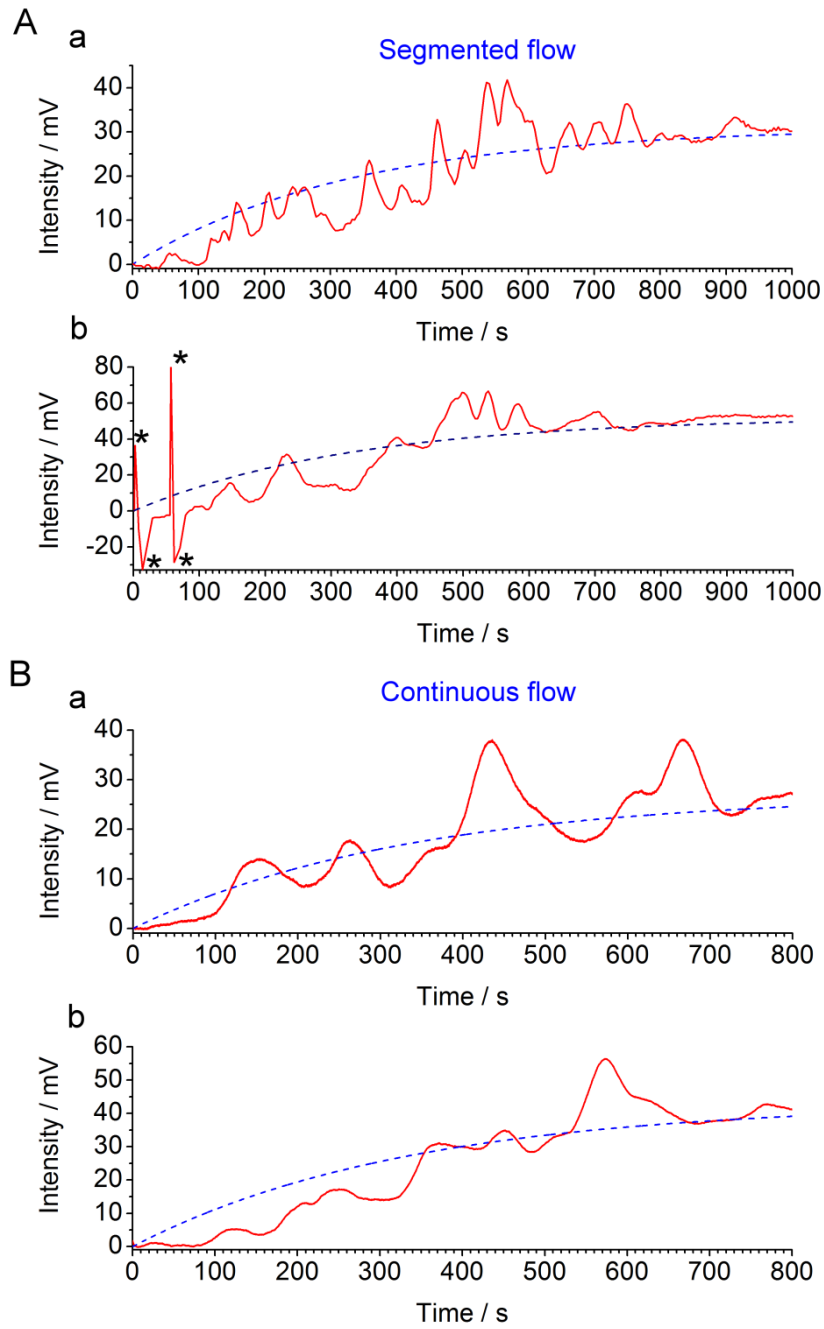


Figure 3.7 Recording convection with segmented and continuous flow. (A) The output data (red line) obtained with the segmented flow sampling (2 replicates). The blue dashed lines correspond to the exponential functions fitted to the experimental data (after removal of *n*-octanol-related features from the trace): a: $f(t) = 31 \times (1 - e^{(-0.003t)})$; b: $f(t) = 52 \times (1 - e^{(-0.003t)})$. The features marked with asterisks (*) are due to air bubbles. (B) The output data (red line) obtained with the continuous flow sampling (2 replicates). The blue dashed lines correspond to the exponential functions fitted to the raw data: a: $f(t) = 27 \times (1 - e^{(-0.003t)})$; b: $f(t) = 43 \times (1 - e^{(-0.003t)})$.

also clear that, at some points, the relative absorbance values (represented by the measured potentials) are much higher than the equilibrium absorbance at the end of the data record. This points out an important feature of convection current; unlike in diffusion, a momentary concentration of the substance in the three-dimensional space may be higher than the concentration of this substance after complete mixing of the substance with the medium. This feature has implications on the real-world convection systems, for example, the release of pollutants to the environment. Overall, the experiments discussed above show the feasibility of sampling convection-induced waves from liquid media on the scale of micro- to millilitres.

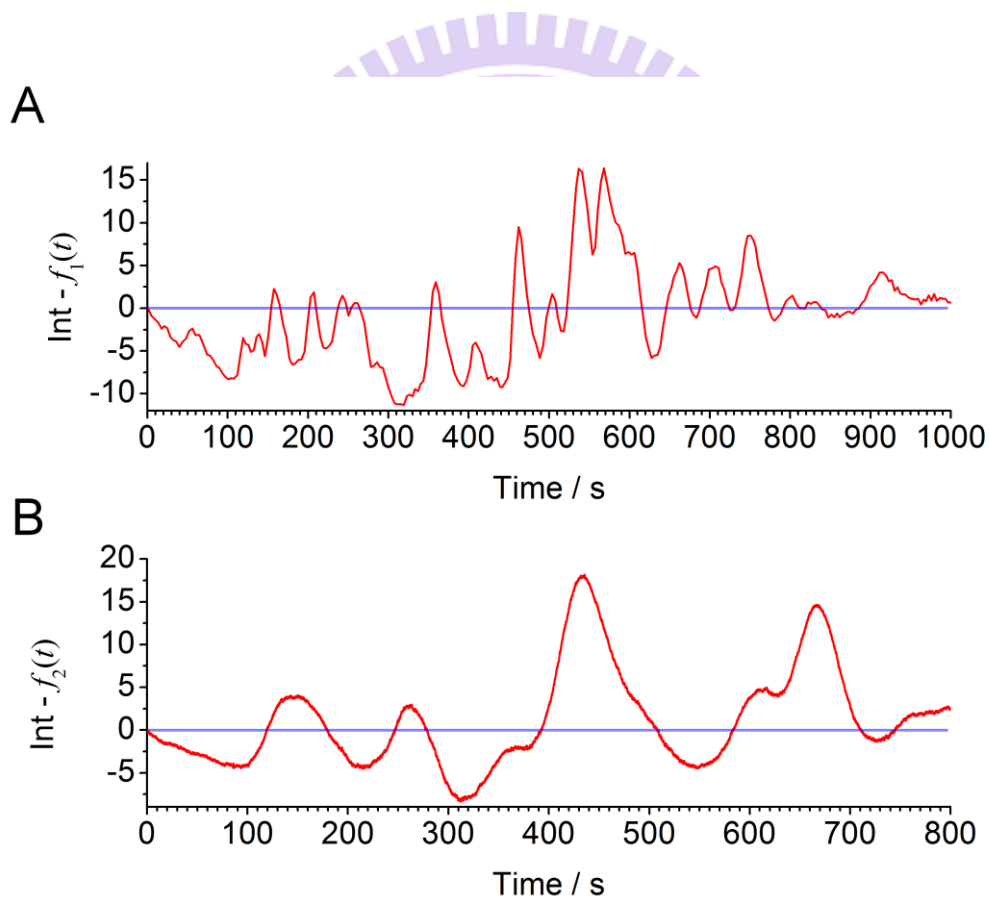


Figure 3.8 An alternative representation of the data sets displayed in **Figure 3.7A** and **3.7B** (upper graphs). The experimental data points were subtracted with the fitted exponential functions (A: $f_1(t) = 31 \times (1 - e^{(-0.003x)})$); B: $f_2(t) = 27 \times (1 - e^{(-0.003x)})$). Fluctuations of absorbance due to convection currents in the glass vial can be clearly seen.

In order to realize the possibility of performing measurements at various wavelengths, offered by the detector described above (*cf.* **Figure 3.1**), we further attempted the monitoring of sequential convection of substances with different absorption maxima (**Figure 3.9**). First, an aliquot of 100 μL of a blue ink was injected into the lower part of the 20-mL glass vial, which was then heated up to induce convection, and segmented flow was then used for sampling (**Figure 3.9A**). The blue ink absorbs green and red light (wavelength range of red: 600-700 nm, green: 490-560) but it does not absorb blue light (wavelength range 450-490 nm, *cf.* **Figure 3.10**). Therefore, one could observe the fluctuating increase of the signal in the detection channels operating at wavelengths 629 and 518 nm (**Figure 3.9A**). Subsequently, a 100- μL aliquot of ferroin was injected into the lower part of the same vial. This time the detection channels operating at wavelengths 518 and 463 nm produced a significant change in the light absorption traces (**Figure 3.9B**).

3.3.2. Monitoring convection-driven currents by optical detector and mass spectrometer

Optical detection benefits from the direct dependence of absorbance on concentration, warranted by the Beer-Lambert law (equation 3, page 8); however, it has poor selectivity. In order to demonstrate the possibility of continuous sampling of chemical waves – such as those due to the convection currents – we have attempted coupling the home-made flow-through optical detector with a mass spectrometer. Several technical problems had to be solved to assure satisfactory performance of the system: One way to improve the temporal resolution of the sampling system is to increase the sampling rate. However, when coupling fluidic systems with MS, it is not desirable to work with high flow rates. Therefore, we have implemented split-flow coupling of the sampling setup with MS via an electrode-free ESI interface. A section of Tygon tubing with a relatively small ID (0.13 μm) was used to produce back pressure (**Figure 3.11A**), and by this way divert a desired fraction of the flow towards the ESI

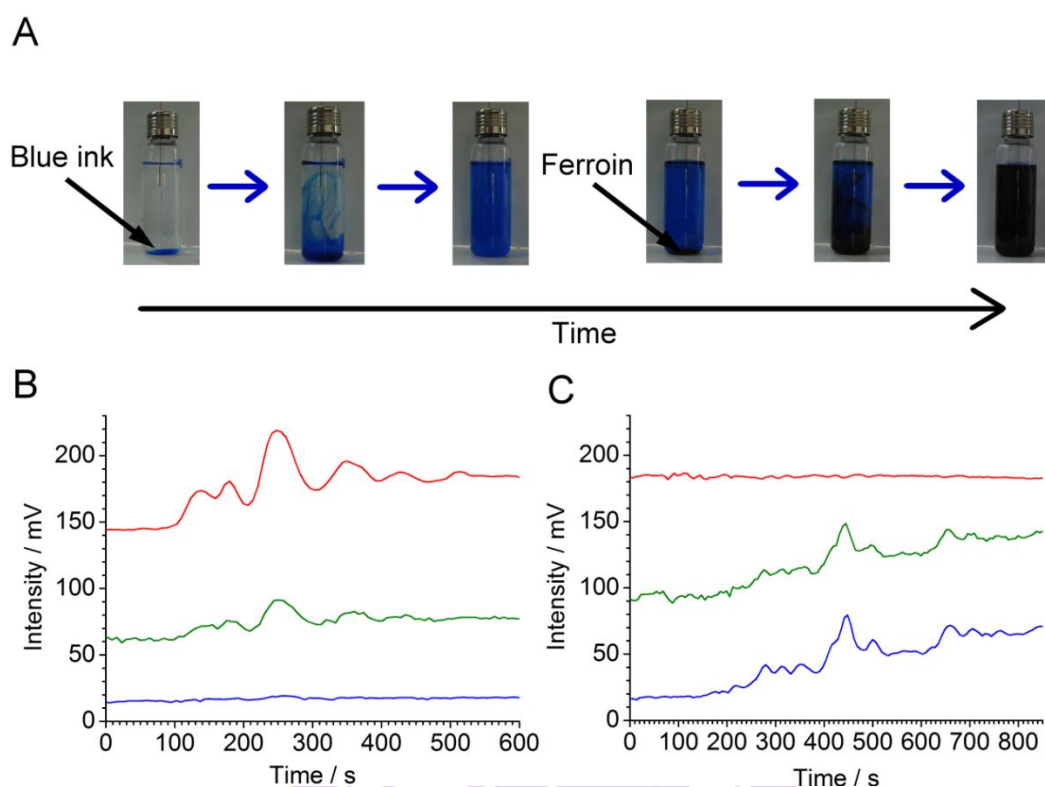


Figure 3.9 Sequential convection of two substances with different visible light absorption maxima. (A) Photographs of the vial (nominal volume: 20 mL) filled with 15 mL of water after injection of blue ink (three pictures to the left), and ferriin (three pictures to the right). (B,C) Sampling and detection of the vial content by segmented-flow used in conjunction with the home-made optical detector (*cf.* **Figure 3.1**). (B) Measurement started after the injection of 100 μL of blue ink (50 \times diluted original sample). (C) Measurement started after subsequent addition of 100 μL of ferriin sample. The delay time between red/green and green/blue channels is ~ 2.5 s. The raw data have been treated with a custom software in order to eliminate the peaks due to the *n*-octanol plugs. Traces were shifted vertically for clarity.

emitter. In this experiment, the nominal flow rate was set to 30 $\mu\text{L min}^{-1}$. The flow rate measured in the fused silica capillary (ESI emitter) was found to be $\sim 6.7 \mu\text{L min}^{-1}$ (**Table 3.1**), which was a satisfactory flow rate for the detection electrospray MS. The flow rate of dry gas was set to 12 L min^{-1} , and the temperature of dry gas was set to 250 $^{\circ}\text{C}$: this helped to assure sufficient desolvation of microdroplets formed at the ESI emitter.

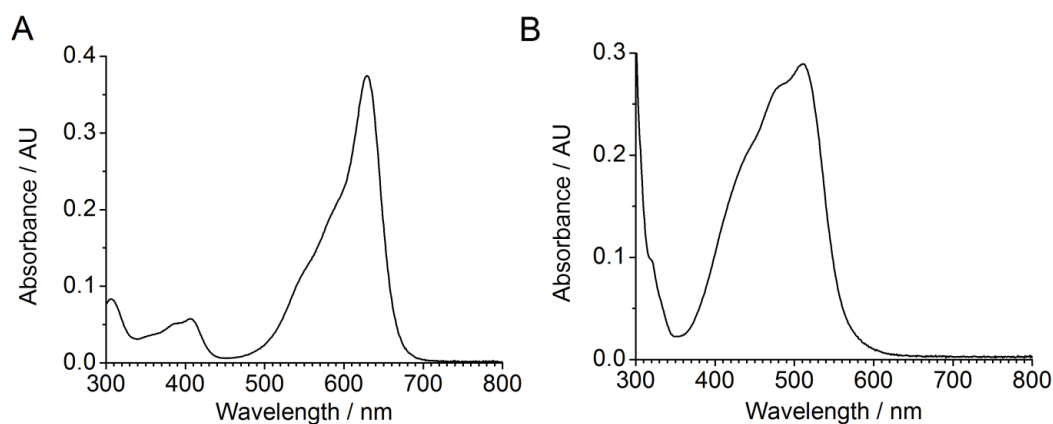


Figure 3.10 UV/Vis absorption spectra of (A) ferrioxalate (2.8×10^{-5} M), and (B) blue ink (1000 \times diluted original solution).

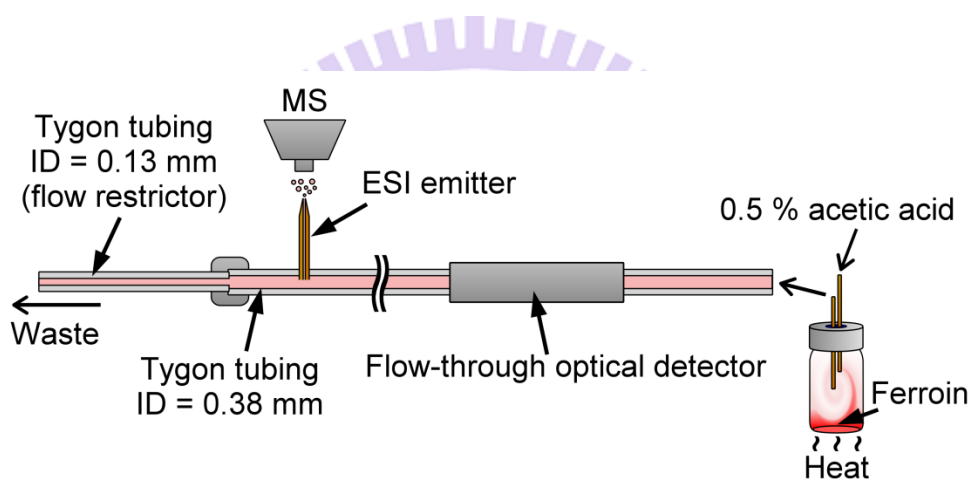


Figure 3.11 Application of the hyphenated system – incorporating the home-made optical detector (*cf.* **Figure 3.1**) and mass spectrometer – in the monitoring of the chemical current due to convection. Nominal volume of the vial volume of the vial is 20 mL. The vial was completely filled with ~ 21 mL the aqueous medium containing the internal standard (caffeine).

Similarly to the previous experiments, a 100- μ L aliquot of ferrioxalate solution was injected into the lower part of a 20-mL glass vial, and the convective mixing was induced by heating (~ 34 $^{\circ}$ C) (**Figure 3.11**). **Figure 3.12A** shows the results obtained by the home-made optical detector (wavelength: 518 nm) as well as the mass spectrometer. In this experiment, caffeine was added to the liquid medium present in the glass vial, and used as an internal standard.

Table 3.1 Measurement of flow rate in the system depicted in **Figure 3.3** by weighing aliquots of water eluted from the flow line (Tygon tubing ID 0.13 mm). Preset flow rate: 30 $\mu\text{L min}^{-1}$. Sample collection time: 10 min.

Replicate No	Sample mass / g		
	MS on	MS off	No ESI emitter
1	0.229	0.271	0.294
2	0.230	0.242	0.293
3	0.228	0.274	0.300
Average	0.229	0.262	0.296
Flow rate at the outlet of the Tygon tubing ($\mu\text{L min}^{-1}$)	22.9	26.2	29.6
Flow rate at the ESI emitter ($\mu\text{L min}^{-1}$)	6.7 (29.6 – 22.9)	3.4 (29.6 – 26.2)	N/A

Figure 3.12B shows the resulting plot representing the intensity ratios of ferriin ($[\text{M}]^{2+}$) and caffeine ($[\text{M}+\text{H}]^+$) peaks at the m/z 298 and 195, respectively. The MS result approximately matches the result obtained from the flow-through optical detector. However, exact matching is hindered by the fact that dispersion and diffusion occur as the sample traverses the flow line section between the optical detector and the ESI emitter, and by possible ionization biases.

3.4. Concluding remarks

We have demonstrated two simple methods for monitoring liquid-phase chemical heterogeneity induced by convection – in millilitre-range volumes – almost in real time. In essence, the three-dimensional chemical waves present in the vial were sampled into a

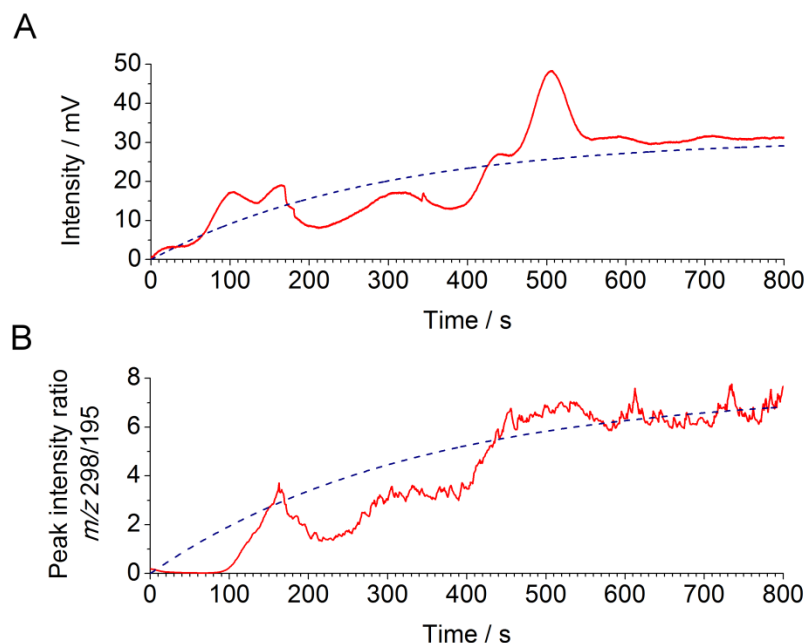


Fig. 3.12 (A,B) Measurement of the relative changes in the concentration of ferriin in the course of convection.

(A) Optical detection; the raw data (red line) were fitted with an exponential function ($f(t) = 31 \times (1 - e^{(-0.0035t)})$), blue line). (B) MS detection; the smoothed data were fitted with an exponential function ($f(t) = 7.5 \times (1 - e^{(-0.0030t)})$), blue line). The data acquisition with MS started 132 s after the start of the data acquisition with the optical detector in order to compensate for the dead-volume delay.

one-dimensional flow line, and transferred to single-point (zero-dimensional) detectors. Harnessing convection-driven currents has potentially huge utility and implications: consider chemical processes that require high concentrations of reactants – in those cases, having a homogeneous reaction mixture would mean the dilution of the reactants. On the other hand, the convection allows one to increase the contact area of the reactants (or one reactant and the catalyst) without considerable dilution of the reactant. We are currently working on several applications for these two methods: they include the monitoring of chemical waves produced in unstirred reaction vessels, spatiotemporal gradients produced by oscillating reactions, and waves of signalling molecules secreted by biological cells. The proposed system can further be developed by hyphenating it with other detectors, including UV absorption detection,

Raman spectroscopy, and microscale nuclear magnetic resonance, and it can potentially be implemented to study other dynamic processes – beyond the convection – for example, dissolution of pharmaceutical preparations.



Chapter 4

Conclusions

In this research work, we have developed two analytical approaches which provide either high spatial resolution or high temporal resolution:

The first study has demonstrated the design, synthesis, and application of a hybrid inorganic-organic nanomaterial for mass spectrometric imaging of single algal cells. The new SiO₂/9-AA nanoparticles can easily be applied to biological specimens by attaching to their outer surface due to electrostatic interactions. Following the attachment, the organic matrix is released from the nanoparticles – in a controlled manner – during the incubation with alkaline vapors. Unlike other matrix coating methods, the proposed approach does not require spraying matrix cocktails over samples. This may help to reduce contamination of the laboratory environment with toxic aerosols. Using these hybrid nanoparticles, the spatial resolution could be down to approximately 15 μm. Therefore, the method enables imaging relatively large cells by MALDI mass spectrometry.

The second study demonstrates the possibility of conducting real-time monitoring of convection currents in segmented and continuous flow systems. The home-made optical detector constructed for the purpose of this study is capable of performing multi-point multi-wavelength absorbance measurements of the samples moving along the flow cell. Using this approach, we were able to observe the development of chaotic chemical currents produced by convection in liquid phase. The continuous-flow sampling system can readily be coupled with an electrospray mass spectrometer. Such a hyphenated system enabled

measurement of chemical waves – induced by convection – by two detectors. We envisage that this approach will further find applications in the monitoring of dynamic chemical systems: not necessarily those related to convection, and not necessarily those involving chromophoric substances.



References

1. Hillenkamp, F.; Peter-Katalinic, J. ed., "MALDI MS: A Practical Guide to Instrumentation, Methods and Applications" 2007, Wiley, Weinheim.
2. Karas, M.; Bachman, D.; Bahr, U.; Hillenkamp, F., "Matrix-Assisted Ultraviolet Laser Desorption of Non-Volatile Compounds" *Int. J. Mass Spectrom. Ion Proc.*, **1987**, 78, 53-68.
3. National High Magnetic Field Laboratory, 2012,
www.magnet.fsu.edu/education/tutorials/tools/ionization_maldi.html.
4. Strupat, K.; Karas, M.; Hillenkamp, F., "2,5-Dihydroxybenzoic acid: a new matrix for laser desorption-ionization mass spectrometry" *Int. J. Mass Spectrom. Ion Proc.*, **1991**, 72, 89-102
5. Chaurand, P.; Luetzenkirchen, F.; Spengler, B., "Peptide and protein identification by matrix-assisted laser desorption ionization (MALDI) and MALDI-post-source decay time-of-flight mass spectrometry" *J. Am. Soc. Mass Spectrom.*, **1999**, 10, 91-103.
6. Beavis, R. C.; Chait, B. T., "Cinnamic acid derivatives as matrices for ultraviolet laser desorption mass spectrometry of proteins" *Rapid Commun. Mass Spectrom.*, **1989**, 3, 432-435
7. Beavis, R. C.; Chait, B. T., "Matrix-assisted laser-desorption mass spectrometry using 355 nm radiation" *Rapid Commun. Mass Spectrom.*, **1989**, 3, 436-439.
8. Beavis, R. C.; Chait, B. T., "High-accuracy molecular mass determination of proteins using matrix-assisted laser desorption mass-spectrometry" *Anal. Chem.*, **1990**, 62, 1836-1840.
9. Vermillion-Salsbury, R. L.; Hercules, D. M., "9-Aminoacridine as a matrix for negative mode matrix-assisted laser desorption/ionization" *Rapid Commun. Mass Spectrom.*, **2002**,

- 16, 1575-1581.
10. Edwards, J. L.; Kennedy R. T., "Metabolomic analysis of eukaryotic tissue and prokaryotes using negative mode MALDI time-of-flight mass spectrometry" *Anal. Chem.*, **2005**, *77*, 2201-2209.
 11. Fuchs, B.; Bischoff, A.; Suss, R.; Teuber, K.; Schurenberg, M.; Suckau, D.; Schiller, J., "Phosphatidylcholines and -ethanolamines can be easily mistaken in phospholipid mixtures: a negative ion MALDI-TOF MS study with 9-aminoacridine as matrix and egg yolk as selected example" *Anal. Bioanal. Chem.*, **2009**, *395*, 2479-2487.
 12. Chang, W. C.; Huang, L. C.; Wang, Y. S.; Peng, W. P.; Chang, H. C.; Hsu, N. Y.; Yang, W. B.; Chen, C. H., "Matrix-assisted laser desorption/ionization (MALDI) mechanism revisited" *Anal. Chim. Acta.*, **2007**, *582*, 1-9.
 13. Sunner, J.; Dratz, E.; Chen, Y-C., "Graphite surface-assisted laser desorption/ionization time-of-flight mass spectrometry of peptides and proteins from liquid solutions" *Anal. Chem.*, **1995**, *67*, 4335-4342.
 14. Kawasaki, H.; Yonezawa, T.; Watanabe, T.; Arakawa, R., "Platinum nanoflowers for surface-assisted laser desorption/ionization mass spectrometry of biomolecules," *J. Phys. Chem. C*, **2007**, *111*, 16278-16283.
 15. Cotter, R. J., "Peer reviewed: the new Time-of-flight mass spectrometry" *Anal. Chem.*, **1999**, *71*, 445A-451A.
 16. Goodwin, R. J.; Pennington, S. R.; Pitt, A. R., "Protein and peptides in pictures: imaging with MALDI mass spectrometry" *Proteomics*, **2008**, *8*, 3785-3800.
 17. Chughtai, K.; Heeren, R. M., "Mass spectrometric imaging for biomedical tissue analysis" *Chem. Rev.*, **2010**, *110*, 3237-3277.
 18. Svatoš, A., "Mass spectrometric imaging of small molecules" *Trends Biotechnol.*, **2010**, *28*, 425-434.
 19. Kaspar, M. Peukert, A. Svatoš, A. Matros, Mock, H-P., "MALDI-imaging mass

- spectrometry — An emerging technique in plant biology” *Proteomics*, **2011**, *11*, 1840-1850.
20. Seeley, E. H.; Caprioli, R. M., “MALDI imaging mass spectrometry of human tissue: method challenges and clinical perspectives” *Trends Biotechnol.*, **2011**, *29*, 136-143.
 21. Goodwin, R. J., “Sample preparation for mass spectrometry imaging: Small mistakes can lead to big consequences” *J. Proteomics*, **2012**, doi: 10.1016/j.jprot.2012.04.012.
 22. Hankin, J. A.; Barkley, R. M.; Murphy, R. C., “Sublimation as a method of matrix application for mass spectrometric imaging” *J. Am. Soc. Mass Spectrom.*, **2007**, *18*, 1646-1652.
 23. Bouschen, W.; Schulz, O.; Eikel, D.; Spengler, B., “Matrix vapor deposition/recrystallization and dedicated spray preparation for high-resolution scanning microprobe matrix-assisted laser desorption/ionization imaging mass spectrometry (SMALDI-MS) of tissue and single cells” *Rapid Commun. Mass Spectrom.*, **2010**, *24*, 355-364.
 24. Yang, J. H.; Caprioli, R. M., “Matrix sublimation/recrystallization for imaging proteins by mass spectrometry at high spatial resolution” *Anal. Chem.*, **2011**, *83*, 5728-5734.
 25. Skoog, D. A.; Holler, F. J.; Grouch, S. R., “Principles of instrumental analysis” **2007**, Thomson Brooks/Cole, Belmont.
 26. Betteridge, D.; Marczewski, C. Z.; Wade, A. P., A “Random walk simulation of flow injection analysis” *Anal. Chim. Acta*, **1984**, *165*, 227-326.
 27. Thorsen, T.; Roberts, R. W.; Arnold, F. H.; Quake, S. R., “Dynamic Pattern Formation in a Vesicle-Generating Microfluidic Device” *Phys. Rev. Lett.*, **2001**, *86*, 4163-4166.
 28. Joanicot, M.; Ajdari, A., “Droplet control for microfluidics” *Science*, **2005**, *309*, 887-888.
 29. Casadevall i Solvas, X.; deMello, A., “Droplet microfluidics: recent developments and future applications” *Chem. Commun.*, **2011**, *47*, 1936-1942.

30. Růžička, J.; Hansen, E. H., "Flow injection analysis" **1988**, Wiley, Weinheim.
31. Song, H.; Chen, D. L.; Ismagilov, R. F., "Reactions in droplets in microfluidic channels" *Angew. Chem. Int. Ed.*, **2006**, *45*, 7336-7356.
32. Chen, D.; Du, W.; Liu, Y.; Liu, W.; Kuznetsov, A.; Mendez, F. E.; Philipson, L. H.; Ismagilov, R. F., "The chemistode: a droplet-based microfluidic device for stimulation and recording with high temporal, spatial, and chemical resolution" *Proc. Natl. Acad. Sci. U.S.A.*, **2008**, *105*, 16843-16848.
33. Wang, M.; Slaney, T.; Mabrouk, O.; Kennedy, R. T., "Collection of nanoliter microdialysate fractions in plugs for off-line in vivo chemical monitoring with up to 2 s temporal resolution" *J. Neurosci. Methods*, **2010**, *190*, 39-48.
34. Slaney, T. R.; Nie, J.; Hershey, N. D.; Thwar, P. K.; Linderman, J.; Burns, M. A.; Kennedy, R. T., "Push-pull perfusion sampling with segmented flow for high temporal and spatial resolution in vivo chemical monitoring" *Anal. Chem.*, **2011**, *83*, 5207-5213.
35. Fenn, J. B.; Mann, M.; Meng, C. K.; Wong, S. F.; Whitehouse, C. M., "Electrospray ionization for mass spectrometry of large biomolecules" *Science*, **1989**, *246*, 64-71.
36. Kebarle, P., "A brief overview of the present status of the mechanisms involved in electrospray mass spectrometry" *J. Mass Spectrom.*, **2000**, *35*, 804-817.
37. Royal Society of Chemistry, "Keeping it together" *Chem. World*, **2003**, www.rsc.org/chemistryworld/Issues/2003/February/together.asp.
38. Smith, R. D.; Loo, J. A.; Edmonds, C. G.; Barinaga, C. J.; Udseth, H. R., "New developments in biochemical mass spectrometry: electrospray ionization" *Anal. Chem.*, **1990**, *62*, 882-899.
39. Bruins, A. P.; Covey, T. R.; Henion, J. D., "Ion Spray interface for combined liquid chromatography/atmospheric pressure ionization mass spectrometry" *Anal. Chem.*, **1987**, *59*, 2642-2646.
40. Cai, J.; Henion, J., "Capillary electrophoresis-mass spectrometry" *J. Chromatogr. A*,

- 1995**, 703, 667-692.
41. R. Graham Cooks, R. G.; Kaiser Jr, R. E., "Quadrupole ion trap mass spectrometry" *Acc. Chem. Res.*, **1990**, 23, 213-219.
 42. Hoffmann, E. D.; Stroobant, V., "Mass spectrometry: principles and applications" **1999**, Wiley, Weinheim.
 43. Shanta, S. R.; Zhou, L.-H.; Park, Y. S.; Kim, Y. H.; Kim, Y.; Kim, K. P., "binary matrix for MALDI imaging mass spectrometry of phospholipids in both ion modes" *Anal. Chem.*, **2011**, 83, 1252-1259.
 44. Urban, P. L.; Chang, C-H.; Wu, J-T.; Chen, Y-C., "Microscale MALDI imaging of outer-layer lipids in intact egg chambers from *Drosophila melanogaster*" *Anal. Chem.*, **2011**, 83, 3918-3925.
 45. Cerruti, C. D.; Benabdellah, F.; Laprevote, O.; Touboul, D.; Brunelle, A., "MALDI imaging and structural analysis of rat brain lipid negative ions with 9-aminoacridine matrix" *Anal. Chem.*, **2012**, 84, 2164-2171.
 46. Caprioli, R. M.; Farmer, T. B.; Gile, J., "Molecular imaging of biological samples: Localization of peptides and proteins using MALDI-TOF MS" *Anal. Chem.*, **1997**, 69, 4751-4760.
 47. Stoeckli, M.; Chaurand, P.; Hallahan, D. E.; Caprioli, R. M., "Imaging mass spectrometry: a new technology for the analysis of protein expression in mammalian tissues" *Nature Med.*, **2001**, 7, 493-496.
 48. Eberlin, L. S.; Liu, X. H.; Ferreira, C. R.; Santagata, S.; Agar, N. Y. R.; Cooks, R. G., "Desorption electrospray ionization then MALDI mass spectrometry imaging of lipid and protein distributions in single tissue sections" *Anal. Chem.*, **2011**, 83, 8366-8371.
 49. Cornett, D. S.; Frappier, S. L.; Caprioli, R. M., "MALDI-FTICR imaging mass spectrometry of drugs and metabolites in tissue" *Anal. Chem.*, **2008**, 80, 5648-5653.
 50. Lunsford, K. A.; Peter, G. F.; Yost, R. A., "Direct matrix-assisted laser

- desorption/ionization mass spectrometric imaging of cellulose and hemicellulose in *Populus* tissue” *Anal. Chem.*, **2011**, *83*, 6722-30.
51. Porta, T.; Grivet, C.; Kraemer, T.; Varesio, E.; Hopfgartner, G., “Single hair cocaine consumption monitoring by mass spectrometric imaging” *Anal. Chem.*, **2011**, *83*, 4266-4272.
52. Khatib-Shahidi, S.; Andersson, M.; Herman, J. L.; Gillespie, T. A.; Caprioli, R. M., “Direct molecular analysis of whole-body animal tissue sections by imaging MALDI mass spectrometry” *Anal. Chem.*, **2006**, *78*, 6448-6456.
53. Zimmerman, T. A.; Rubakhin, S. S.; Romanova, E. V.; Tucker, K. R.; Sweedler, J. V., “MALDI Mass spectrometric imaging using the stretched sample method to reveal neuropeptide distributions in aplysia nervous tissue” *Anal. Chem.*, **2009**, *81*, 9402-9409.
54. Vrkoslav, V.; Muck, A.; Cvacka, J.; Svatoš, A., “MALDI imaging of neutral cuticular lipids in insects and plants” *J. Am. Soc. Mass Spectrom.*, **2010**, *21*, 220-231.
55. Trepte, J.; Bottcher, H., “Improvement in the leaching behavior of dye-doped modified silica layers coated onto paper or textiles,” *J. Sol-Gel Sci. Techn.*, **2000**, *19*, 691-694.
56. Unger, B.; Rurack, K.; Muller, R.; Resch-Genger, U.; Buttke, K., “Effects of the sol-gel processing on the fluorescence properties of laser dyes in tetraethoxysilane derived matrices” *J. Sol-Gel Sci. Techn.*, **2000**, *19*, 799-802.
57. Laperriere, S. C.; Mullens, J. W.; Lesperance, D.; Chronister, E. L., “Optical-energy transfer and trapping in 9-aminoacridine doped sol-gel Ggasses” *Chem. Phys. Lett.*, **1995**, *243*, 114-124.
58. Baylson, F. A.; Stevens, B. W.; Domozych, D. S., “Composition and synthesis of the pectin and protein components of the cell wall of *Closterium acerosum* (Chlorophyta),” *J. Phycol.*, **2001**, *37*, 796-809.
59. Baluya, D. L.; Garrett, T. J.; Yost, R. A., “Automated MALDI matrix deposition method with inkjet printing for imaging mass spectrometry” *Anal. Chem.*, **2007**, *79*, 6862-6867.

60. Mazutis, L.; Baret, J. C.; Treacy, P.; Skhiri, Y.; Araghi, A. F.; Ryckelynck, M.; Taly, V.; Griffiths, A. D., "Multi-step microfluidic droplet processing: kinetic analysis of an in vitro translated enzyme" *Lab chip*, **2009**, *9*, 2902-2908.
61. Cai, L-F.; Zhu, Y.; Du, G-S.; Fang, Q., "Droplet-based microfluidic flow injection system with large-scale concentration gradient by a single nanoliter-scale injection for enzyme inhibition assay" *Anal. Chem.*, **2012**, *84*, 446-452.
62. Roach, L. S.; Song, H.; Ismagilov, R. F., "Controlling nonspecific protein adsorption in a plug-based microfluidic system by controlling interfacial chemistry using fluorinated-phase surfactants" *Anal. Chem.*, **2005**, *77*, 785-796.
63. Martino, C.; Zagnoni, M.; Sandison, M. E.; Chanasakulniyom, M.; Pitt, A. R.; Cooper, J. M., "Intracellular protein determination using droplet-based immunoassays" *Anal. Chem.*, **2011**, *83*, 5361-5368.
64. Miller, O. J.; El Harrak, A.; Mangeat, T.; Baret, J-C.; Frenz, L.; El Debs, B.; Mayot, E.; Samuels, M. L.; Rooney, E. K.; Dieu, P.; Galvan, M.; Link, D. R.; Griffiths, A. D., "High-resolution dose-response screening using droplet-based microfluidics" *Proc. Natl. Acad. Sci. U.S.A.*, **2012**, *109*, 378-383.
65. Shim, J-U.; Olguin, L. F.; Whyte, G.; Scott, D.; Babbie, A.; Abell, C.; Huck, W. T.; Hollfelder, F., "Simultaneous determination of gene expression and enzymatic activity in individual bacterial cells in microdroplet compartments" *J. Am. Chem. Soc.*, **2009**, *131*, 15251-15256.
66. Gu, S-Q.; Zhang, Y-X.; Zhu, Y.; Du, W-B.; Yao, B.; Fang, Q., "Multifunctional picoliter droplet manipulation platform and its application in single cell analysis" *Anal. Chem.*, **2011**, *83*, 7570-7576.
67. Kautz, R. A.; Goetzinger, W. K.; Karger, B. L., "High-throughput microcoil NMR of compound libraries using zero-dispersion segmented flow analysis" *J. Comb. Chem.*, **2005**, *7*, 14-20.

68. Hatakeyama, T.; Chen, D. L.; Ismagilov, R. F., "Microgram-scale testing of reaction conditions in solution using nanoliter plugs in microfluidics with detection by MALDI-MS" *J. Am. Chem. Soc.*, **2006**, *128*, 2518-2519.
69. Pei, J.; Li, Q.; Kennedy, R. T., "Rapid and label-free screening of enzyme inhibitors using segmented flow electrospray ionization mass spectrometry" *J. Am. Soc. Mass Spectrom.*, **2010**, *21*, 1107-1113.
70. Song, P.; Hershey, N. D.; Mabrouk, O. S.; Slaney, T. R.; Kennedy, R. T., "Mass spectrometry "sensor" for *in vivo* acetylcholine monitoring" *Anal. Chem.*, **2012**, *84*, 4659-4664.
71. Sun, S.; Slaney, T. R.; Kennedy, R. T., "Label free screening of enzyme inhibitors at femtomole scale using segmented flow electrospray ionization mass spectrometry" *Anal. Chem.*, **2012**, *84*, 5794-5800.
72. Hsieh, C-H.; Chang, C-H.; Urban, P. L.; Chen, Y-C., "Capillary action-supported contactless atmospheric pressure ionization for the combined sampling and mass spectrometric analysis of biomolecules" *Anal. Chem.*, **2011**, *83*, 2866-2869.
73. Trojanowicz, M. ed., "Advances in Flow Analysis" **2008**, Wiley, Weinheim.